PNNL-26789

Pacific Northwest
NATIONAL LABORATORY

Proudly Operated by Battelle Since 1965

Refinement of Gamma Spectroscopy Methods for Unattended UF_6 Cylinder Verification

September 2017

LE Smith
JA Kulisek
J Webster
MA Zalavadia
R Guerrero
BS McDonald

Prepared for the U.S. Department of Energy
under Contract DE-AC05-76RL01830

PACIFIC NORTHWEST NATIONAL LABORATORY
operated by
BATTELLE
for the
UNITED STATES DEPARTMENT OF ENERGY
under Contract DE-AC05-76RL01830

Printed in the United States of America

Available to DOE and DOE contractors from the
Office of Scientific and Technical Information,
P.O. Box 62, Oak Ridge, TN 37831-0062;
ph: (865) 576-8401
fax: (865) 576-5728
email: reports@adonis.osti.gov

Available to the public from the National Technical Information Service
5301 Shawnee Rd., Alexandria, VA 22312
ph: (800) 553-NTIS (6847)
email: orders@ntis.gov <http://www.ntis.gov/about/form.aspx>
Online ordering: http://www.ntis.gov

This document was printed on recycled paper.
(8/2010)

PNNL-26789

Refinement of Gamma Spectroscopy Methods for Unattended UF_6 Cylinder Verification

LE Smith
JA Kulisek
J Webster
MA Zalavadia
R Guerrero
BS McDonald

September 2017

Prepared for
the U.S. Department of Energy
under Contract DE-AC05-76RL01830

Pacific Northwest National Laboratory
Richland, Washington 99352

Abstract

In recent years, the International Atomic Energy Agency (IAEA) has pursued innovative techniques and an integrated suite of safeguards measures to address the verification challenges posed by the front end of the nuclear fuel cycle. Among the methods currently being explored by the IAEA is automated, independent verification of the declared enrichment, ^{235}U mass, total uranium mass and identification of declared UF_6 cylinders in a facility (e.g., uranium enrichment plants and fuel fabrication plants). Under the auspices of the U.S. Support Program to the IAEA, Phase I of the Unattended Cylinder Verification Station (UCVS) project was completed in October 2016. During the Phase I final review (October 2016) and subsequent discussions, several technical questions were raised, the answers to which were important to the planning and early stages of Phase II. Under funding by the US National Nuclear Security Administration Office of International Nuclear Safeguards, Pacific Northwest National Laboratory (PNNL), Los Alamos National Laboratory, and Oak Ridge National Laboratory performed technical investigations aimed at some of these questions. PNNL led the studies regarding adaptation of gamma-spectroscopy methods to better align with the envisioned geometries of the integrated Phase II UCVS prototypes, and to improve performance for unattended enrichment verification via the 186-keV signature—particularly for cylinders at natural and depleted enrichments. This report summarizes the work performed by PNNL in these and other areas during FY17. The findings reported here have and will inform decisions about gamma-ray spectrometer type(s), module designs and analysis methods to be deployed in Phase II of the UCVS project.

Acknowledgments

Funding for this work has been provided by the U.S. National Nuclear Security Administration's (NNSA) Office of Nonproliferation and Arms Control (NA-24) Office of International Nuclear Safeguards (OINS).

Acronyms and Abbreviations

PNNL	Pacific Northwest National Laboratory
HEVA	Hybrid Enrichment Verification Array
ROI	Region of Interest
MCNP	Monte Carlo N-Particle
ADC	Analog to Digital Conversion
MCA	Multi-Channel Analyzer
DTB	Digital Tube Base
FWHM	Full Width Half Maximum
LLD	Lower Level Discriminator
PHA	Pulse Height Analysis
PUR	Pile-Up Rejection
LTC	Live-Time Correction
FT	Flat-top Time
RT	Rise Time

Contents

Figures

Tables

1.0 Introduction

In recent years, the International Atomic Energy Agency (IAEA) has pursued innovative techniques and an integrated suite of safeguards measures to address the verification challenges posed by the front end of the nuclear fuel cycle (Cooley 2007)(Lebrun 2009)(Smith 2013). Among the unattended instruments currently being explored by the IAEA is an Unattended Cylinder Verification Station (UCVS) that could provide automated, independent verification of the declared relative enrichment, ^{235}U mass, total uranium mass and identification for all declared UF_6 cylinders in a facility (e.g., uranium enrichment plants and fuel fabrication plants). Toward this goal, the U.S. Support Program to the IAEA funded a team consisting of Pacific Northwest National Laboratory (PNNL), Los Alamos National Laboratory (LANL), Oak Ridge National Laboratory (ORNL) and Savannah River National Laboratory (SRNL) to complete Phase I of a UCVS viability study. Phase I was completed in October 2016; scope, methods and findings were documented in the UCVS Phase I final report (Smith 2016).

A key outcome of UCVS Phase I was a quantitative performance evaluation of two candidate NDA methods, the Hybrid Enrichment Verification Array (HEVA) and the Passive Neutron Enrichment Meter (PNEM). The two methods were compared using cylinder occupancies from over 200 "typical" Type 30B cylinders. The viability of PNEM and HEVA signatures to support the concept of an "NDA Fingerprint" (to periodically verify that the contents of a given cylinder are consistent with previous scans) was also investigated using several series of repeated cylinder occupancies under specific conditions designed to address key technical questions. A modeling study, combined with field-measured instrument uncertainties, assessed the material-diversion sensitivity of HEVA and PNEM for both one-time assay and (repeated) NDA Fingerprint verification scenarios.

The Phase I results showed that both HEVA and PNEM are highly capable NDA methods, either of which could substantially improve on the today's handheld methods in terms of assay precision, full-volume interrogation and material-substitution sensitivity. Further, the results indicated that there is significant complementarity in the gamma-ray and neutron signatures. A central recommendation from Phase I was the need for an investigation of an NDA method that merges a higher-fidelity gamma-ray signature (e.g., using $LaBr_3$ instead of NaI(Tl)) with neutron signatures collected using ^3He tubes. This merger has several facets, including hardware, data acquisition software, and analysis methods.

In terms of hardware, the indirect HEVA neutron signature will be dropped in favor of the more-precise singles neutron signature from PNEM. This means that the collimator design used in the gamma-ray modules can be more conventional and compact, and the gamma-ray modules can be deployed in more versatile geometric configurations that can for example, accommodate both Type 30B and Type 48 cylinders. In terms of analysis, the independent gamma-ray and neutron approaches will be comparable to Phase I, but their hybridization will be studied in more depth and with an eye toward implementation automation and adaptability (e.g., different weighting of neutron and gamma-ray signatures as a function of declared enrichment).

Reflecting the merging of the candidate NDA methods, the terms "PNEM" and "HEVA" will not be used beyond the already completed Phase I. Instead, the signatures under study in the merged method will be referred to as $UCVS_{EM}$ (enrichment meter based on 186-keV), $UCVS_S$ (Singles neutron), and $UCVS_D$ (Doubles neutron). In addition, the term "NDA Fingerprint" will no longer be used; instead, the term Content Re-Verification (CRV) will be used. These vocabulary changes have been adopted in this report.

During the UCVS Phase I final review (October 2016) and subsequent discussions, several technical questions were raised, the answers to which were important to the early planning and proposal stages for Phase II. Under funding by the US National Nuclear Security Administration (NNSA) Office of International Nuclear Safeguards, PNNL, LANL and ORNL performed technical investigations aimed at some of these questions, including:

- Adaptation of gamma-spectroscopy methods to reduce wall-deposit effects in $UCVS_{EM}$ (PNNL as lead);
- Enhanced neutron methods to mitigate systematic uncertainties in $UCVS_S$ and $UCVS_D$ (LANL as lead);
- Scoping of a notional Phase II data analysis workflow (LANL as lead);
- Phase I load-cell performance (ORNL as lead).

The products of these separate but connected FY17 "bridge studies" at PNNL, LANL and ORNL have fed directly into preparations for UCVS Phase II, beginning with the proposal submitted to the USSP and the IAEA in July 2017.

This report summarizes the FY17 activities devoted to the first topic above. This work has been performed by PNNL but was aligned with the FY17 scope at LANL and ORNL. The report is organized to be consistent with the various tasks undertaken by PNNL in FY17:

- Enhancement of MCNP modeling and simulation tools for gamma-ray signatures, benchmarked by Phase I field data, to support specific technical investigations;
- Re-design of the UCVS gamma-ray module to reflect envisioned configurations for the integrated Phase II UCVS prototypes that will include NDA, load cells, cylinder ID and surveillance;
- Comparative study of candidate gamma-ray spectrometer types (NaI(Tl), $LaBr_3$, CZT) for the enrichment meter method in UCVS configurations, using a library of MCNP-simulated spectra;
- Preliminary exploration of NaIGEM as a candidate gamma-ray spectrometry analysis algorithm, using primarily Phase I data collected with NaI(Tl) spectrometers;
- Preliminary investigation of the multi-parameter Content Reverification (CRV) concept (formerly, "NDA Fingerprint"), building from the limited data and testing in Phase I.

2.0 MCNP Modeling and Simulation

Radiation transport modeling and simulations were conducted to address a variety of objectives in preparation for UCVS Phase II. The first objective was to increase the understanding of gamma-ray signature variation presented by cylinders with relatively high levels of wall deposits and/or heels (hereafter "heels" for simplicity") in UCVS assay configurations. This was accomplished by comparing simulated cylinder assays with the Phase I measurements taken with the HEVA NaI(Tl) (hereafter "NaI") detectors. Once it was shown that the simulated HEVA NaI spectra were consistent with field-measured cylinders, the MCNP models were used to support several other analysis objectives. One of these objectives was to model the effects of cross-talk, a scenario for which nearby cylinders generate extraneous signatures in the gamma-ray detectors, thereby increasing, particularly, the down-scattered continuum in the spectra collected from the cylinder being assayed. A study was also conducted to optimize the design of a tungsten (W) collimator for the notional UCVS Phase II gamma-ray module. Yet another use of the MCNP modeling was to generate synthetic $LaBr_3$ (hereafter "LaBr") and cadmium zinc telluride (CZT) spectra representing a range of cylinder characteristics (e.g., clean to heavy heels, enrichments from depleted to 5 wt%) that could be used to support a comparative study of predicted performance for gamma-ray spectrometers under consideration for Phase II. Each of these topics is discussed in the subsections that follow.

2.1 As-modeled Design of UCVS Prototype and Gamma-ray Modules

In the modeling of the gamma-ray modules envisioned for Phase II, it is assumed that the nominal configuration is clamshell in form for both gamma-ray and neutron modules (see Figure 1 left). Such a design is expected to be appropriate for both UCVS variants called out by the IAEA for Phase II: 1) stand-alone platform capable of accommodating Type 30B and Type 48 cylinders, and 2) modular configuration capable of integrating with operator equipment (e.g., accountancy scale or trolley). Under these assumptions, compactness is a key factor in the design process. To achieve compactness in a clamshell configuration, the Phase II gamma-ray modules will use a side-looking detector orientation that aligns easily with the neutron pods (Figure 1 left). A preliminary model of the UCVS Phase II neutron modules was also produced and included in gamma modeling for completeness; however, the neutron response was not investigated by PNNL in the gamma-ray-focused simulation studies described in this report. A report from LANL documents potential advancements for the singles and neutron signature measurements in Phase II (Broughton 2017).

While the Phase II gamma-ray modules are the focus of the modeling effort described in this report, the NaI-based HEVA modules deployed in Phase I were also modeled in order to support benchmarking to Phase I field data, as well as performance-comparison studies between the Phase I gamma-ray module and those envisioned for Phase II. The right pane of Figure 1 depicts the locations of the Phase I HEVA modules (one with NaI, as deployed in Phase I, labeled HEVA-NaI; the other with a hypothetical LaBr for simulation-based performance comparisons, labeled HEVA-LaBr) and Phase II UCVS gamma-ray modules, all mounted on a model of the as-built, stand-alone UCVS platform deployed in the Phase I field trial (Smith 2016).

A total of four Phase II gamma-ray modules were included in this modeling study. These two pairs of Phase II gamma-ray modules were modeled at opposite ends of the UCVS Phase II neutron modules (Figure 1, left pane). A cross-sectional diagram of all detector models, in their appropriate positions within the UCVS

model, is shown in the right image of Figure 1. The LaBr crystal used in all models was cylindrical with a diameter of 3.81 cm and a thickness of 3.81 cm. The CZT detectors simulated in the Phase II gamma-ray modules were modeled according to manufacturer specifications, with a quasi-hemispherical shape having a volume of approximately 1500 mm^3 (Ivanov 2015). Each pair of Phase II gamma-ray modules on either side of the Phase II neutron modules faced away from each other, and their LaBr crystals were oriented sideways such that the circumferential edge of the crystals faced the UF_6 cylinder. For the CZT crystals, one of the sides with the larger of the two areas faced the cylinder, through the collimator aperture.

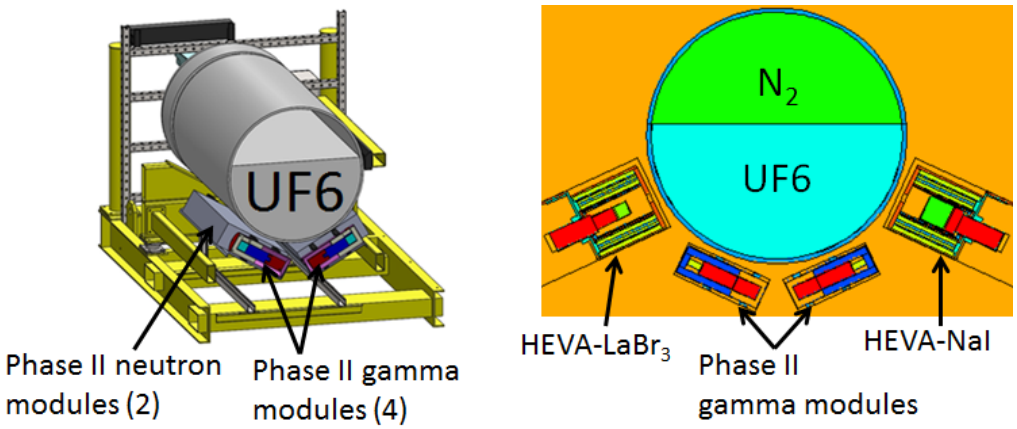

Figure 1. Left: Notional, as-modeled design of the Phase II stand-alone UCVS platform variant, including two neutron modules and four gamma-ray modules in a clamshell configuration. Right: cross-section of all gamma-ray detector models used in the MCNP modeling, including Phase I HEVA modules with as-deployed NaI and hypothetical LaBr spectrometers.

A comparison of detector characteristic parameters for the modeled detector is provided in Table 1. Two different energy resolution functions were used in the model for the LaBr detector. One of these functions was determined from recent measurements made on a LaBr detector purchased by PNNL for the UCVS project. The other energy resolution function was determined from prior measurements made on a LaBr detector at Idaho National Laboratory (INL) (Kulisek 2007). The latter had better resolution at low energies and therefore represents a best-case scenario for LaBr. As shown in Table 1, the 1.5 cm^3 CZT detector has the highest energy resolution, followed by LaBr, which in turn is followed by NaI. The CZT detector, however, was the smallest in size and therefore had the lowest detection efficiency. The area of the surface of the CZT detector facing the cylinder was 5.4 times smaller than that of the LaBr detector and 21.7 times smaller than the NaI detector. Furthermore, the CZT detector crystal had thickness of only 0.72 cm, which was 5.3 times lower than that of the LaBr detector and 10.6 times lower than that of the NaI detector. This is reflected in the CZT's lower peak/total ratio reported in Table 1 for the 662 keV photopeak generated from a simulated measurement of a ^{137}Cs source. (Worth noting is that the gap between the peak/total ratios for the LaBr and CZT spectrometers narrows at the 186-keV energy of most interest in the enrichment-meter method.) Only the LaBr detector was modeled in the collimator design study described in section 1.3. However, synthetic spectra were generated for the CZT in that same collimator configuration, as described in section 1.4, to support performance comparisons for the enrichment-meter method in assay geometries consistent with UCVS Phase II planning.

Modeling the response function of CZT detectors is non-trivial since CZT detectors exhibit a pronounced low-energy tailing effect in their gamma-ray spectra that can be attributed to the trapping of holes within

the CZT crystal (Schlesinger 2001). This degrades the spectroscopic capabilities of CZT. While high-quality spectroscopy grade CZT with associated electronics specifically designed for superior spectroscopic performance may have tailing levels less than 10%, the commercially available spectrometers used by the IAEA today and likely to be deployed in the UCVS would presumably have tailing levels greater than 50% (Richter and Siffert 1992, Sokolov et al. 2008). To afford flexibility in the choice of CZT tailing and energy-resolution behavior, PNNL developed an algorithm that allows "tuning" of the tailing characteristics, as measured by FWHM and FWTM of the 662-keV and 186-keV peaks, to specific values. The algorithm used the un-broadened pulse-height MCNP tally as input, and convolved it with an empirically-determined sum of two Gaussians to account for the hole-tailing observed in CZT detectors. For this study, those specific tailing characteristics were taken from a study performed by the IAEA and its collaborators that compared the performance of several commercially available spectrometers, including CZT crystals of various sizes, for enrichment-meter assay of UF_6 (Ivanov 2015). More specifically, the response function for CZT used in this study was tuned to the performance reported by the IAEA for the Ritec Microspec1500, one of the larger commercially available CZT spectrometers at approximately 1.5 cm^3.

Table 1. Comparison of NaI, LaBr, and CZT detector performance parameters.

Detector	Incident Area (cm^2)	FWHM (keV) @ 186 keV	FWTM (keV) @ 186 keV	FWHM (keV) @ 662 keV	FWTM (keV) @ 662 keV	peak/total @ 662 keV
HEVA NaI	45.6	23.2	42.6	47.2	89.8	0.47
Phase II LaBr (PNNL)	11.4	10.8	19.8	20.2	37.1	0.40
Phase II LaBr (INL)	11.4	8.9	16.4	18.6	34.2	0.40
Phase II CZT	2.1	6.0	14.4	10.4	31.1	0.20

Two aperture designs were investigated for the tungsten collimator of the notional Phase II gamma-ray modules. The straight aperture design is shown in the left image of Figure 2, and the divergent collimator design is shown in the right image of Figure 2. The divergent collimator had the same 3-cm diameter circular aperture at the inner wall of the tungsten as the straight collimator, but diverged outward in a cone at an angle of 45 degrees. This divergent collimator design yielded an increase in count rate of approximately 20% over the straight collimator design and with no noticeable distortion in the gamma-ray spectrum (e.g., increased down-scatter continuum), but for simplicity in design and fabrication, a straight collimator was implemented in the prototype modules. To ensure significant flexibility in terms of field of view and managing count rates in the spectrometers, a set of aperture plugs with various diameters (described later) was implemented.

In all of the models, the UF_6 filled 60% of the cylinder volume, which is the maximum allowable fill level (United States Enrichment Corporation 2006) and is typical of Type 30B cylinders in the field. A heel of UF_6 was modeled as a thin layer plated along the inner cylinder wall. Gamma rays from the uranium decay products in the heel, from previous UF_6 fills, were emitted in the simulation to compare with spectra from

Phase I measurements having high net count rates within the 766 keV and 1001 keV ^{234m}Pa photopeaks and their concomitant continuum.

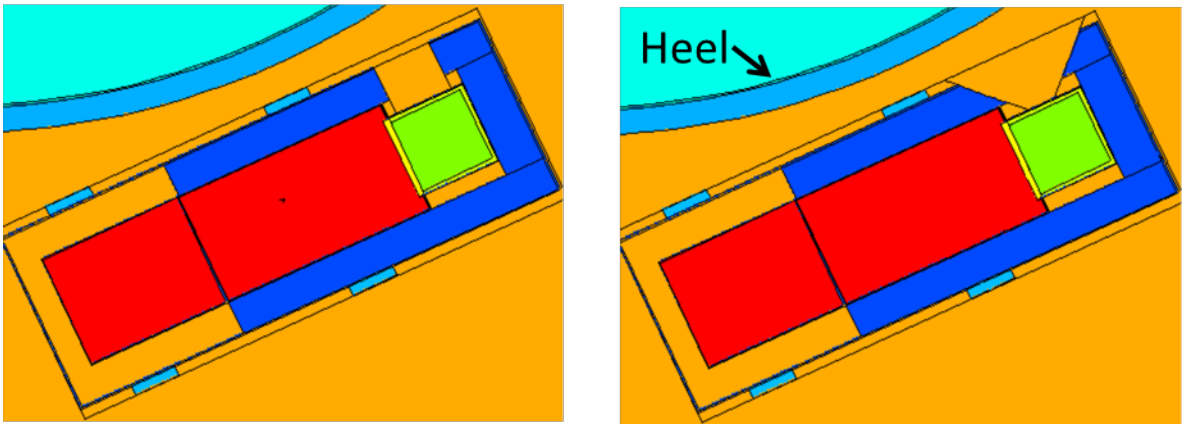

Figure 2. Cross-section of the straight (left image) and divergent (right image) tungsten aperture designs investigated for the LaBr-based Phase II gamma-ray modules.

2.2 Benchmarking of Naturally-Enriched Heels Cylinders

Energy spectra of the naturally-enriched (NU) UF_6 cylinders that were recorded from measurements made with individual HEVA-NaI modules, during the Westinghouse Fuel Fabrication Facility (WFFF) field trial in Phase I, are shown in Figure 3. The spectrum with the lowest gross count rate is labeled "CYL1". The spectrum with the second-highest gross count rate is labeled "CYL2", and the spectrum with the highest gross count rate is labeled "CYL3". The CYL1 and CYL3 spectra used in this benchmarking were measured using the middle HEVA module in the Phase I prototype (HEVA-2 in the Phase I final report). The CYL2 spectrum was collected with the Phase I HEVA module furthest from the cylinder nameplate (HEVA-3 in the Phase I final report). The acquisition time for all three spectra was approximately 7 minutes. As shown, these three spectra are very different not only in terms of count rate but in the continuum shape underneath the 186-keV ROI.

Previous studies have also reported high variability among gamma-ray spectra collected from cylinders with heels (Walton 1974) (Smith 2014). The effect of heels on gamma-ray spectra depends on the age of the UF_6, time since last cleaning, and the enrichment level of previous cylinder fillings since it was last cleaned (Smith 2016). The volume and mass of heels, the uranium based compounds and ^{238}U progeny on the bottom and walls of the cylinder, generally grow with the number of fillings that a given cylinder has experienced. Per cylinder certification regulations, cylinders must be cleaned of such material once its mass exceeds 11.3 kg (United States Enrichment Corporation 2006).

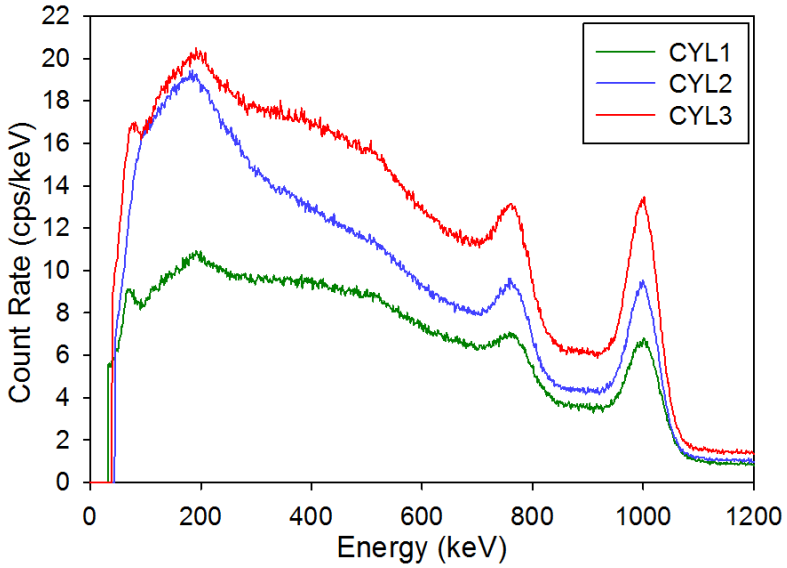

Figure 3. Energy spectra of natural cylinders taken from measurements made with individual HEVA-NaI modules during the WFFF field trial in Phase I.

The simulated response of the HEVA-LaBr detector module is also shown in the graphs that follow within this section. These LaBr spectra, shown in Figure 4 through Figure 8, were broadened to match the resolution versus energy characteristic of the LaBr detector that was characterized previously at INL.

The MCNP model of the HEVA-NaI depicted in Figure 1 (right, denoted HEVA-2-NaI in this section) was used to support the benchmarking against the spectra from the Phase I measurements shown in Figure 3. This benchmarking analysis served a variety of other modeling objectives. For instance, agreement between simulation and measurement results gives confidence in using simulations to optimize detector design. The benchmarking also ensures that the synthetic spectra generated for other types of detectors, such as LaBr and CZT, are reasonably tied to reality.

The benchmarking process developed by PNNL was based on the simulation of individual spectral components, and a fitting algorithm to combine those components in proportions that provide the best agreement with the as-measured spectra. The three spectral components included in the process were: 1) clean cylinder with no heels or wall deposits; 2) heels and wall deposits only; and 3) background presented by a cylinder sitting near the UCVS prototype during the assay of the NU cylinder. Each of these components, and the process for their combination, are described below.

The simulated spectra for a perfectly clean, naturally-enriched UF_6 (NU) cylinder with no heel is shown in Figure 4, for the two HEVA variants and the side-looking LaBr module envisioned for Phase II. These spectra were generated using both gamma-ray and neutron source terms from ^{235}U and ^{238}U, along with their radioactive decay daughter products—assuming a cylinder age of at least 6 months so that the daughter products are in equilibrium. Clear from the two LaBr spectra is that the down-scatter continua under the 186-keV peaks are somewhat higher in the HEVA module design, due to the relatively high volume of low-Z materials (i.e., iron and polyethylene to encourage HEVA's indirect neutron signature) in that collimator design, versus the high-Z tungsten collimator envisioned for the Phase II gamma-ray modules. The 186-keV peak signal is also higher, due to the larger effective field of view in the new design.

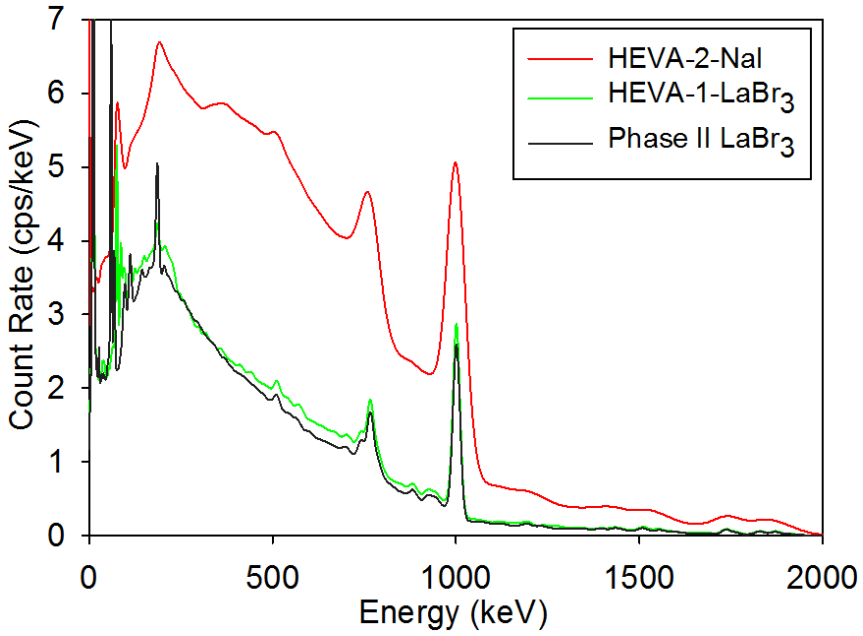

Figure 4. Simulated spectra for a naturally-enriched, clean cylinder more than 6 months after filling so that the ^{238}U daughters are in equilibrium.

The simulated spectra for the heel component are shown in Figure 5. These spectra consist of the same ^{235}U and ^{238}U source terms as the bulk UF_6 but by far the dominant contribution to this heels spectral component is the gamma rays and bremsstrahlung from ^{234m}Pa, a daughter of ^{238}U. This concentration of ^{234m}Pa is generated within the bulk UF_6 in a clean cylinder as the UF_6 ages and is assumed to be entrained in place until the cylinder is emptied. When the cylinder is emptied via cylinder heating and pressure reduction, only the uranium hexafluoride sublimes and escapes and therefore, all of the ^{234m}Pa and ^{234}Th, its parent, from this previous UF_6 filling is assumed to remain plated against the cylinder wall. This heels source term presents a significant spectral signature to subsequent assays of that cylinder, after refilling (Walton, 1974). The magnitudes of the heels spectra shown in Figure 5 are for a heel that is left in the cylinder immediately after the UF_6 cylinder is emptied (prior to decay of the uranium daughters), and therefore represents a worst case scenario in terms of maximum heels spectral contribution. In practice, the radiation source term from the heel will decrease with time after cylinder re-filling, such that its contribution to the overall gamma-ray spectrum is negligible after a period of 6 months. This is the time required for ^{234}Th, the immediate parent of ^{234m}Pa, to decay to 0.5% of its original amount (half-life of 24.1 days).

In its most simple form, the process for generating a simulated cylinder spectrum was to combine the bulk-only, clean-cylinder component for NU with a heels-only component (as exemplified in Figure 4 and Figure 5, respectively), with a scaling coefficient on the heel spectrum determined using linear least squares regression. That is, a single fitted coefficient for each cylinder determined the scalar magnitude of the combined contribution from the bremsstrahlung, 766 keV, and 1001 keV source terms from the heel. This cylinder-specific heel spectrum was then superimposed upon the fixed spectrum contribution from a pure, clean cylinder filled with NU (aged to 6 months). By way of example, the heels magnitude coefficient for a perfectly clean cylinder aged to 6 months would be zero; for the CYL1 and CYL3 cylinders used in this benchmarking exercise, the heel magnitude coefficients were 0.052 and 0.12 respectively. As discussed later, a slightly different process was used for CYL2.

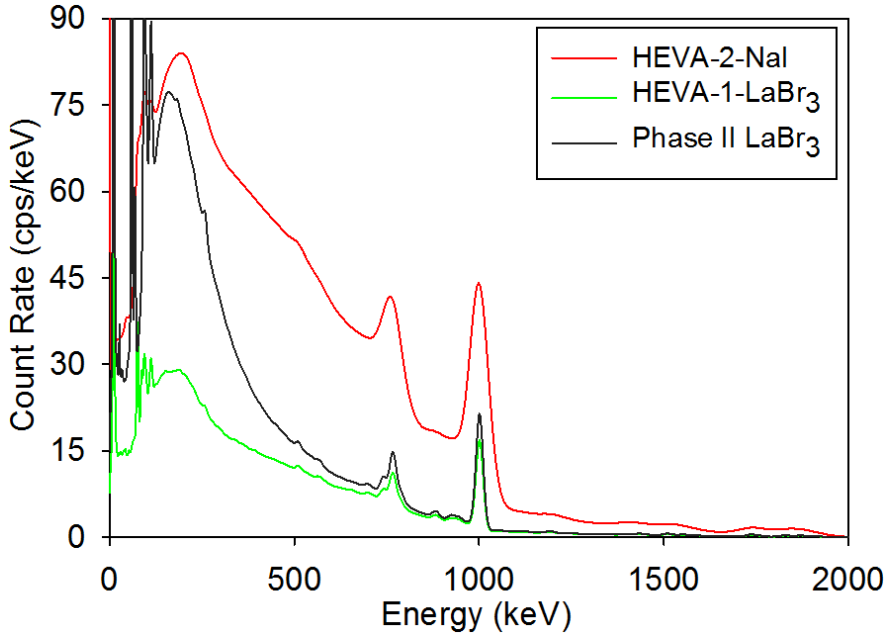

Figure 5. Simulations of the gamma-ray spectral component generated by the heel (uranium daughter products) that remains after emptying a full Type 30B cylinder, assuming that the UF_6 aged at least six months before between initial filling and emptying.

Results are shown in Figure 6 comparing the simulated HEVA-NaI spectrum to the spectrum from the measurement taken with the Phase I middle HEVA module, of the cleanest (CYL1) of the three benchmarked cylinders. The total measured gross count rate in the HEVA-module was 7.8 kcps, as compared to the simulated rate of 7.9 kcps. As noted in the annotations, the bremsstrahlung contribution from the heel, based on the least-squares fitting method described above, was approximately 70% of the contribution from the bulk UF_6, and the gamma-ray peaks at 766 keV and 1001 keV had a contribution from the heel that was roughly half that of the bulk UF_6. The larger ratio for the bremsstrahlung is consistent with the fact that the higher-energy signatures from the discrete gamma-ray lines undergo less attenuation in the bulk material, on the path to the detectors.

While the 186 keV photopeak cannot be distinguished in the NaI spectra of Figure 6, it is distinctly visible within the simulated HEVA-1-LaBr spectrum. It is important to note that all of the simulated spectra have significantly more statistical precision than expected for UCVS assay scenarios in which occupancy times are likely to be 5 minutes or less. For example, the simulated HEVA-1-LaBr spectra shown in Figure 6 has a statistical precision equivalent to that expected for a 3.9-hr assay time, as compared to approximately 7 minutes for the measured data.

Figure 7 provides a comparison of the simulated and measured spectra for the cylinder with the highest count rate (CYL3) of the three benchmarked cylinders. The total measured gross count rate in the middle Phase I HEVA module was 14.6 kcps and the simulated rate was 14.2 kcps, both of which are approximately twice the rate of CYL1, reflecting the much higher heels source term in this NU cylinder. The bremsstrahlung contribution from the heel is now 2.5 times greater than from the UF_6 bulk, and the gamma-

ray line contribution from the heel is approximately 1.6 times higher than the bulk UF_6. Even for this cylinder with the most radioactive heel, the 186 keV photopeak can still be distinguished in the simulated HEVA-1-LaBr spectrum. However, it is important to note again that the simulated spectra (both LaBr and NaI) have the statistical precision equivalent to that of a 3.9-hr assay.

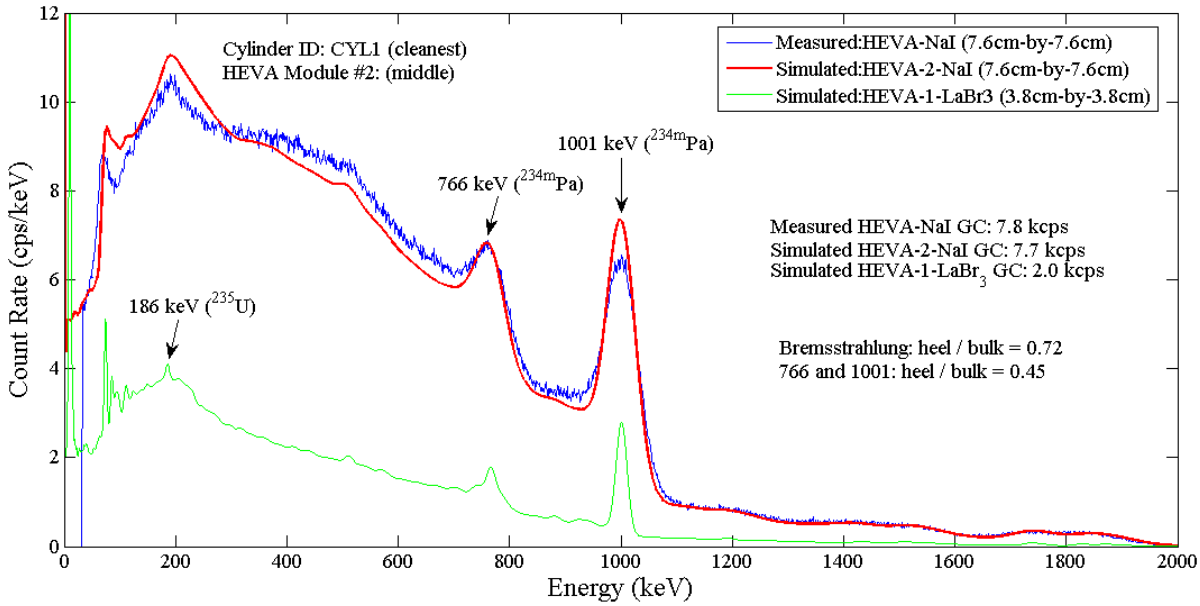

Figure 6. Simulated and measured spectra in response to the cleanest cylinder (CYL1) of the three benchmark cylinders measured during the Phase I field trial. The simulated spectra have the statistical precision of a 3.9-hr assay; the measured spectrum had a 7-minute occupancy duration.

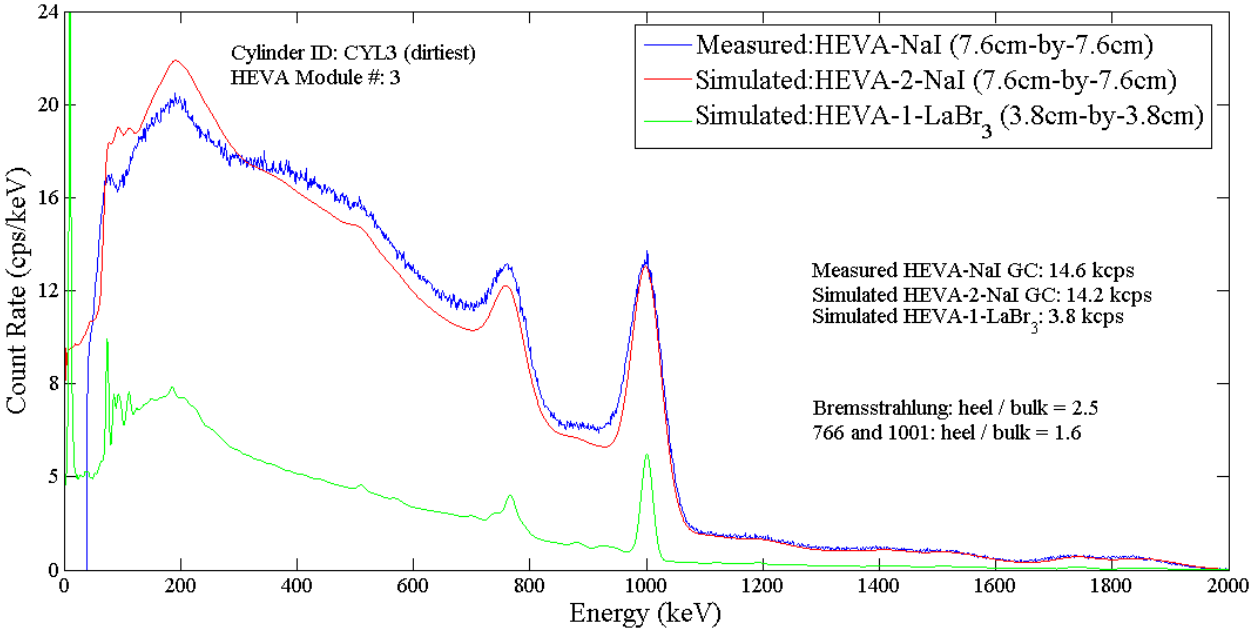

Figure 7. Simulated and measured spectra in response to the cylinder (CYL3) with the greatest count rate among the three NU benchmark cylinders measured during the Phase I field trial. The simulated spectra have the statistical precision of a 3.9-hr assay; the measured spectrum had a 7-minute occupancy duration.

Results are shown in Figure 8 comparing the simulated HEVA-2-NaI spectrum to the spectrum collected with the outer Phase I HEVA module (i.e., furthest from the nameplate), on the cylinder with the middle count rate (CYL2) of the three benchmarked cylinders. As indicated in Figure 3, the shape of the continuum under the 186-keV peak for this cylinder was distinctly different from the continua shapes for CYL1 and CYL3. Because of this difference, the simple "clean cylinder + heel" fitting approach used to produce the simulated CYL3 NaI spectrum is not as effective as it was for CYL1 and CYL3. There appears to be another source term or perturbing effect in CYL2 that needs consideration.

In an effort to explore potential explanations for this difference in continuum shape, another set of simulations was conducted to determine the effects from a far-field cylinder placed at a distance of 3 meters from the outer wall of the assay cylinder and behind the simulated HEVA-2-NaI module in the MCNP model, as shown in Figure 9. This is intended to represent a cylinder sitting in the driveway behind the UCVS prototype during the WFFF field trial, and outside the view of the surveillance camera used to determine whether occupancies had been perturbed by nearby cylinder movements (Smith 2016). The far-field cylinder was modeled with an enrichment of 4.95 wt% ^{235}U with a heels component. It was discovered in the model that the vast majority of the contribution from the far-field cylinder was not from gamma rays streaming through the backside of the HEVA module, but rather from gamma rays that scattered off the assay cylinder and entered through the front face of the HEVA-2-NaI module, a process which is illustrated in Figure 9.

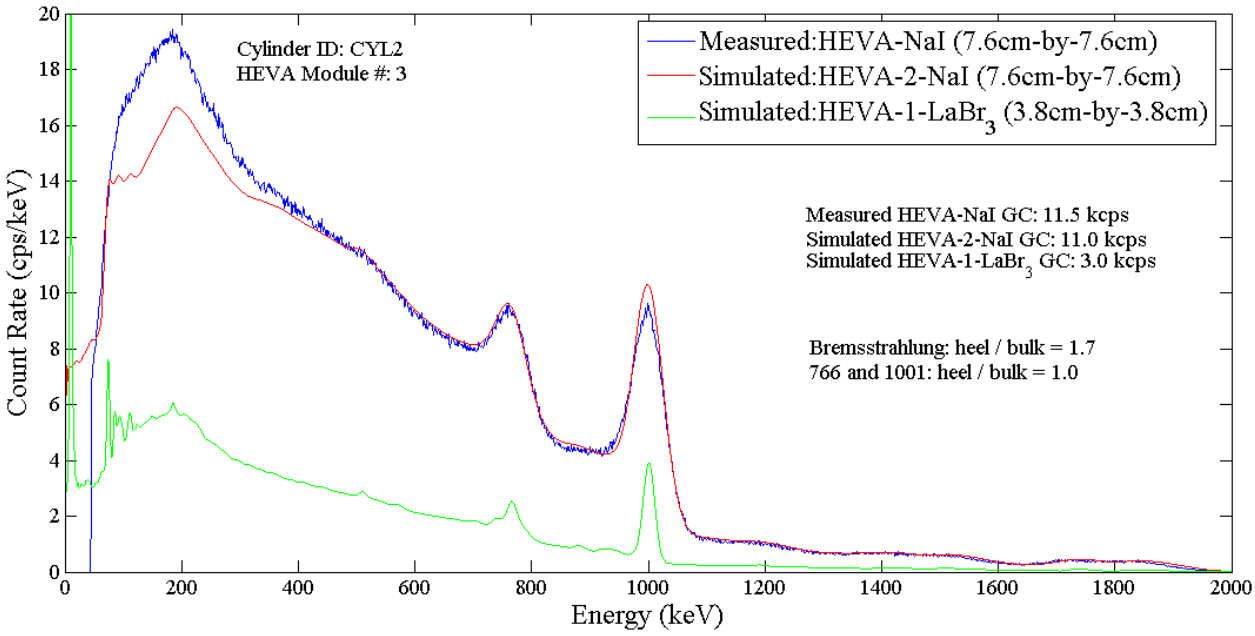

Figure 8. Simulated and measured spectra in response to the cylinder (CYL2) with the middle count rate among the three benchmark cylinders measured during the Phase I field trial. The simulated spectra were produced using only the clean-cylinder and heel source terms, as in Figures 6 and 7 for CYL1 and CYL3. Simulated responses have the statistical precision of a 3.9-hr assay; the measured spectrum had a 7-minute occupancy duration.

The simulated responses of the HEVA NaI and LaBr to the assay cylinder, far-field cylinder, and combined assay cylinder and far-field cylinder are shown in Figure 10. The simulation results shown in Figure 10 were generated by fitting the simulated bulk and heel components to the data from the outer HEVA module in the Phase I prototype (i.e., HEVA-3 in the Phase I report). In the fitting process for the simulated spectra, the scalar magnitudes of both the heels components of the assay and far-field cylinders were used as the two free parameters in the fit (as opposed to only the heels component from the assay cylinder, as was done for Figures 6, 7 and 8). It was determined that a combination of a clean NU cylinder (i.e., no heel, fitting coefficient of 0.0) plus the far-field cylinder contribution shown in Figure 10 is in much better agreement with the measured spectrum than when only the source term from heels in the assay cylinder is considered as a free variable (Figure 8).

While simulation indicates that a nearby cylinder may have produced the somewhat different continuum shape in CYL2, the video feed from the Phase I field trial did not indicate the presence of any cylinders behind the HEVA array during CYL2 occupancy. However, the video feed was not continuous in that it did not capture every instant in time, and the field of view was such that a cylinder sitting 3 m behind the UCVS platform may have been outside of the field of view. The true source of the different underlying continuum shape remains unknown. It can only be said that the modeled scenario of a far-field cylinder sitting behind the HEVA array during the CYL2 occupancy can plausibly explain the spectral shape that was observed.

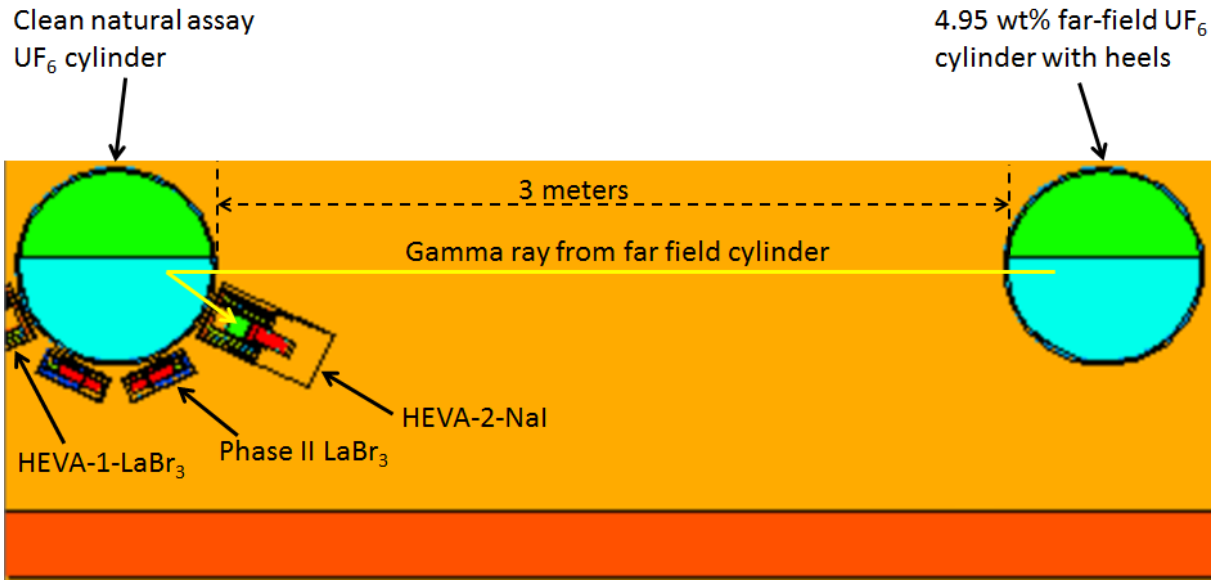

Figure 9. MCNP model of a clean, natural assay cylinder along with a far-field cylinder 3 meters away (enrichment of 4.95wt%).

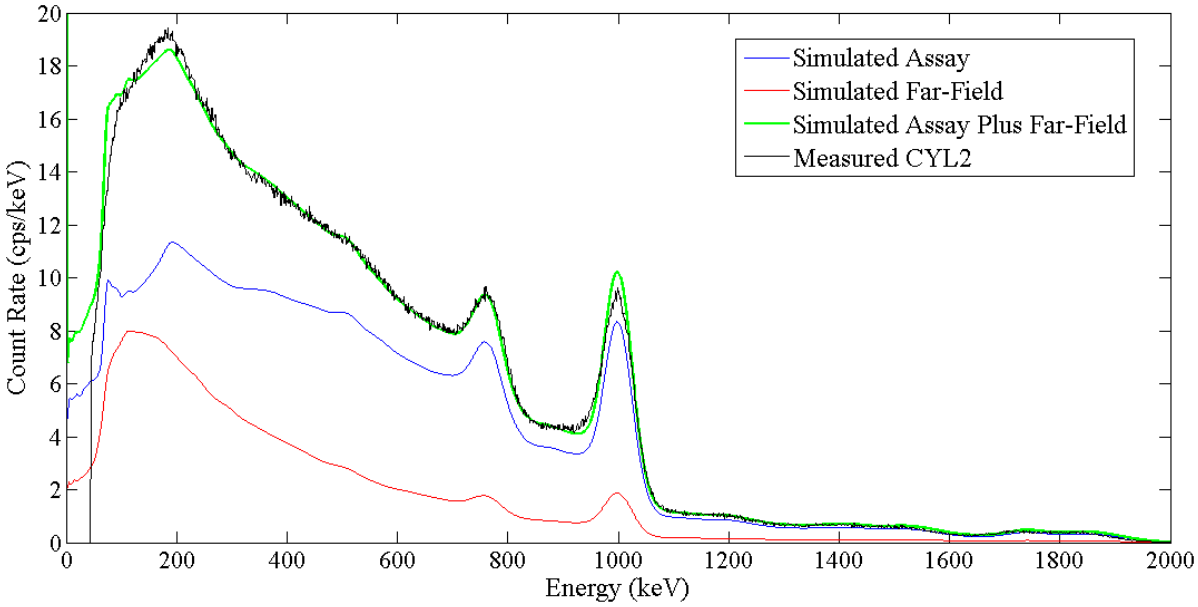

Figure 10. Simulated HEVA-2-NaI spectrum generated from a clean assay cylinder (NU) with cross-talk interference from a nearby far-field cylinder (4.95wt%), as compared to the measured spectrum for NU cylinder CYL2. No heel component was included in the green spectrum; simulated responses have the statistical precision of a 3.9-hr assay; the measured spectrum had a 7-minute occupancy duration.

3.0 Phase II Gamma-ray Module Prototypes

As described above, a clamshell configuration for the gamma-ray modules is envisioned for Phase II, and both LaBr and CZT are candidate spectrometer types for those modules. PNNL has designed, fabricated and tested an initial prototype module design that assumes LaBr as the spectrometer type but that can be modified to accommodate a CZT spectrometer, should that be the preferred sensor for Phase II. This section describes the MCNP simulations and analysis that supported the initial module design, the characteristics of the as-built LaBr modules, and results of initial laboratory testing on those modules. Some aspects of the Phase I HEVA modules were retained in the LaBr prototype modules, including the use of the Canberra Osprey to provide high voltage, preamplifier, shaping amplifier and other pulse-processing features, as described fully in a previous PNNL report (Zalavadia 2016).

3.1 Gamma-ray module Collimator Design Study

MCNP modeling and simulations were performed in order to enhance the design of a tungsten collimator surrounding Phase II spectrometers (e.g., LaBr crystals). Parametric studies were conducted to accomplish this by determining the gross count rates and energy spectral shapes for varying collimator lengths and thicknesses. In these simulations, the total mass of the collimator was limited to 22.7 kg (50 lbs.), which is a typical workplace safety limit for manually lifting objects. In addition, a modeling and simulation analysis was conducted to determine whether a 1-mm copper cap would need to be included in the final design to shield the Phase II LaBr crystals from tungsten x-rays generated in the collimator.

3.1.1 Copper Surrounding LaBr

Modeling and simulations were conducted to determine the effects of adding a 1-mm copper cap around the Phase II LaBr crystal in order to shield it from x-rays produced in the surrounding tungsten collimator. For these simulations, ^{235}U photons were emitted only from the heel for simplicity, since the primary objective was to determine whether the tungsten x-rays would interfere with the 185.7 keV photopeak from ^{235}U. The results of this analysis are shown in Figure 11. As shown in this figure, the copper cap significantly reduces the magnitude of the 59 keV and 67.5 keV tungsten x-ray peaks. However, these x-ray peaks are well-separated from the 185.7 keV ^{235}U photopeak such that they are unlikely to produce peak interference, even at NaI energy resolution. In addition, the tungsten x-ray peaks may prove quite useful for energy calibration in the UCVS, particularly for low-enrichment cylinders where confident location of the 186-keV peak can be challenging with automated algorithms. Yet another factor is that the copper cap reduces the peak magnitude of the 185.7 keV photopeak by 14%, thereby diminishing an already weak signature in the NU and DU cylinders. Because overall count rates in the LaBr module will be modest (i.e., less than 50 kcps even for the highest enrichment cylinders with high heels), the additional count rate from the x-rays should not produce any degrading pulse pileup effects.

Though the measured spectra from real cylinders are much more complex and challenging to analyze than the idealized spectrum in Figure 11, the potential for the tungsten x-rays to aid energy calibration and the desire to enhance the 186-keV signal as much as possible, encourages a collimator design that does not include copper shielding between the tungsten and the detector, or a copper cap on the detector.

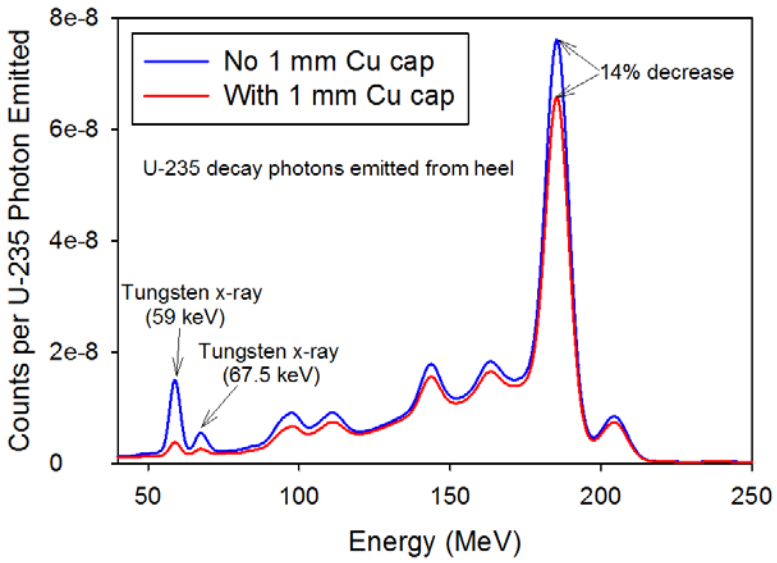

Figure 11. Counts per ^{235}U photon emitted from the heel, with and without a 1-mm copper cap surrounding the Phase II LaBr crystal.

3.1.2 Collimator Thickness Parametric Analysis

The MCNP model used in the tungsten collimator thickness parametric analysis is shown in Figure 12. The tungsten collimator, shown in dark blue in Figure 12, was modeled with a uniform thickness surrounding the entire perimeter of the Phase II gamma-ray module. The thickness of the tungsten collimator was varied in the simulations. For this analysis, the input source definition to the MCNP simulation were gamma rays emitted from the heel, mostly from ^{238}U daughters (e.g., ^{234m}Pa), since this is the most penetrating source component.

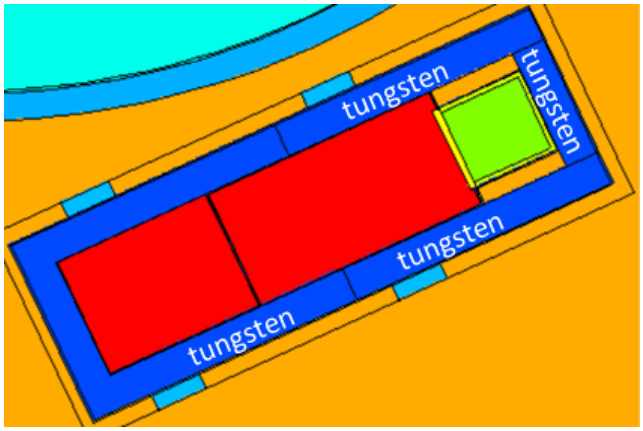

Figure 12. Model of the Phase II gamma-ray module used in the collimator thickness parametric analysis.

Results are shown in Figure 13 illustrating the gross count rate, per photon emitted from the heel, versus the thickness of the tungsten collimator. The overall gross count rate from a photon energy deposition between 40 keV and 5 MeV is shown, as well as the gross count rate within the HEVA traditional region-

of-interest (ROI) between 130 and 215 keV that includes the 185.7 keV photopeak. The as-built thickness is 1.74 cm of tungsten surrounding the outer diameter of the PMT. At this thickness, the overall gross count rate from the heel gamma-rays is estimated to be 6.7% of the overall gross count rate with no collimator, and the count rate within the traditional ROI is 3% of the traditional ROI gross count rate with no collimator. Full energy spectra are shown in Figure 14 for selected tungsten thicknesses ranging from 0.5 cm to 2.0 cm in increments of 0.5 cm. These results indicate that the as-built thickness of 1.74 cm will be sufficient to significantly reduce the spectral continuum under the 185.7 keV ROI used in the enrichment meter method, while balancing the need to keep module mass at a reasonable value.

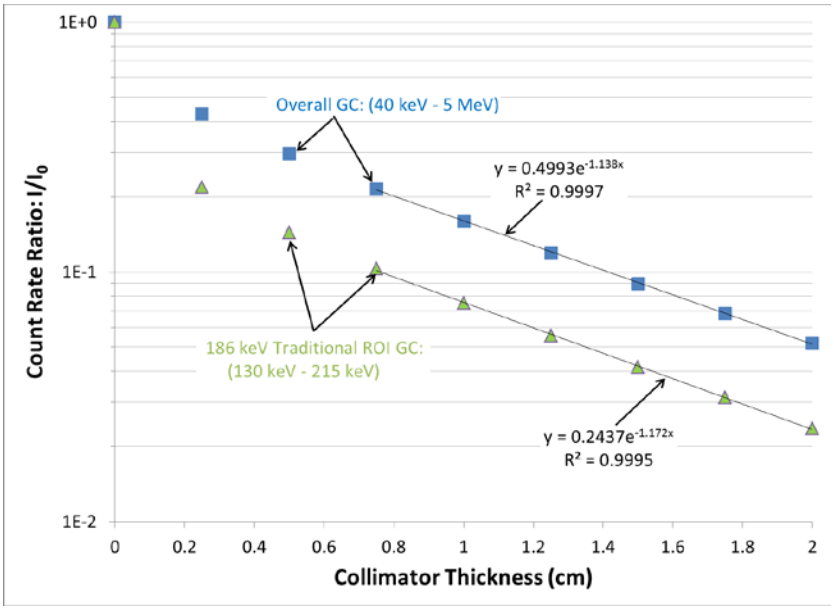

Figure 13. Gross count rate overall and within the traditional ROI versus collimator thickness.

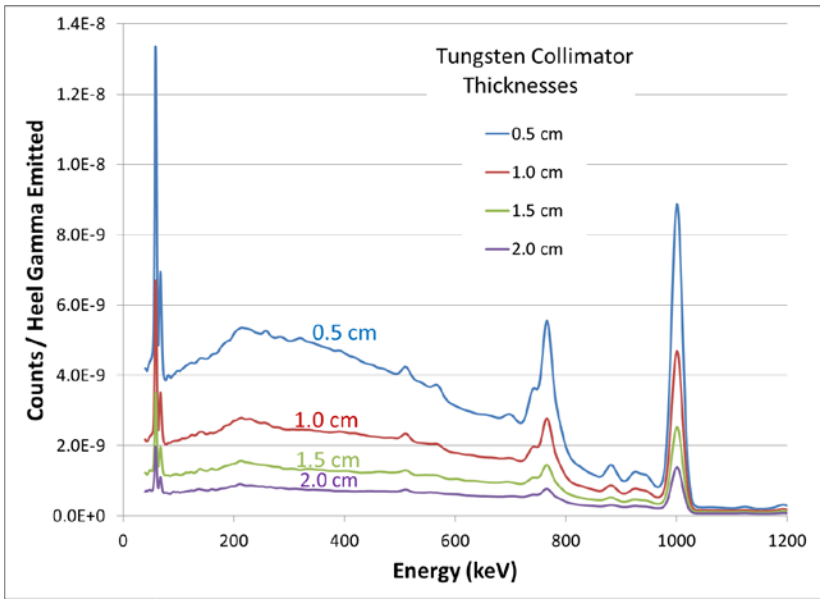

Figure 14. Phase II LaBr spectra versus uniform collimator thickness.

3.1.3 Collimator Length Parametric Analysis

The MCNP model used in parametric analysis for the length of the tungsten collimator length is shown in the left image of Figure 15, for which the extension beyond the LaBr crystal was varied in the simulations. The tungsten collimator shown in Figure 15 extends 7 cm beyond the base of the LaBr crystal, which results in a total Phase II gamma-ray module mass of approximately 18 kg (40 lbs.), assuming a 1.7-cm collimator thickness as defined in the previous section. For this analysis, the input source definition to the MCNP simulation were gamma rays emitted from the heel, mostly from ^{238}U daughters (e.g., ^{234m}Pa), since this is the most penetrating source component.

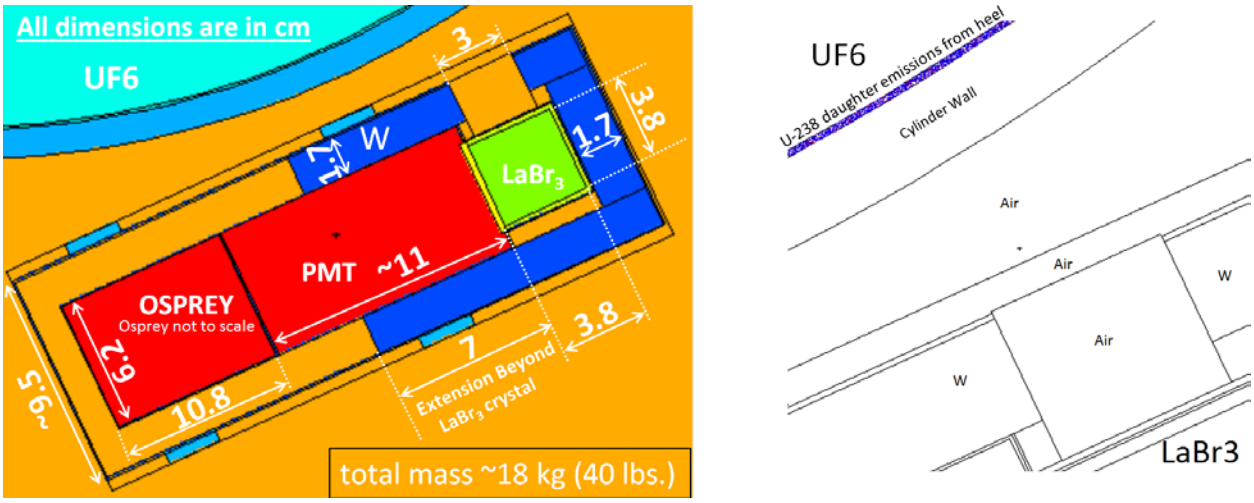

Figure 15. Left: Dimensions of Phase II gamma-ray module assumed in the collimator length parametric analysis. Right: Gamma rays, mostly from ^{238}U daughters, were emitted from the heel for this analysis.

Results are shown in Figure 16 illustrating the gross count rate, per photon emitted from the heel, versus the length of the tungsten collimator in terms of its extension beyond the LaBr crystal (see Figure 15). A dotted line in Figure 16 indicates the as-built collimator length of 8 cm extension beyond the LaBr crystal. At this length, the simulated count rate was only 4% greater than the minimum count rate at the maximum collimator length. Results are shown in Figure 17, in terms of the photon current entering the LaBr crystal across the surface connected to the PMT (see Figure 15). This back current is 14% greater at the final, as-built collimator length than the minimum back current at the maximum collimator length. The 8-cm collimator extension beyond the LaBr crystal was implemented in the as-built prototype gamma-ray module for Phase II since it seemed to strike a suitable balance between achieving most of the attenuation benefits while simultaneously seeking to reduce the weight of the collimator.

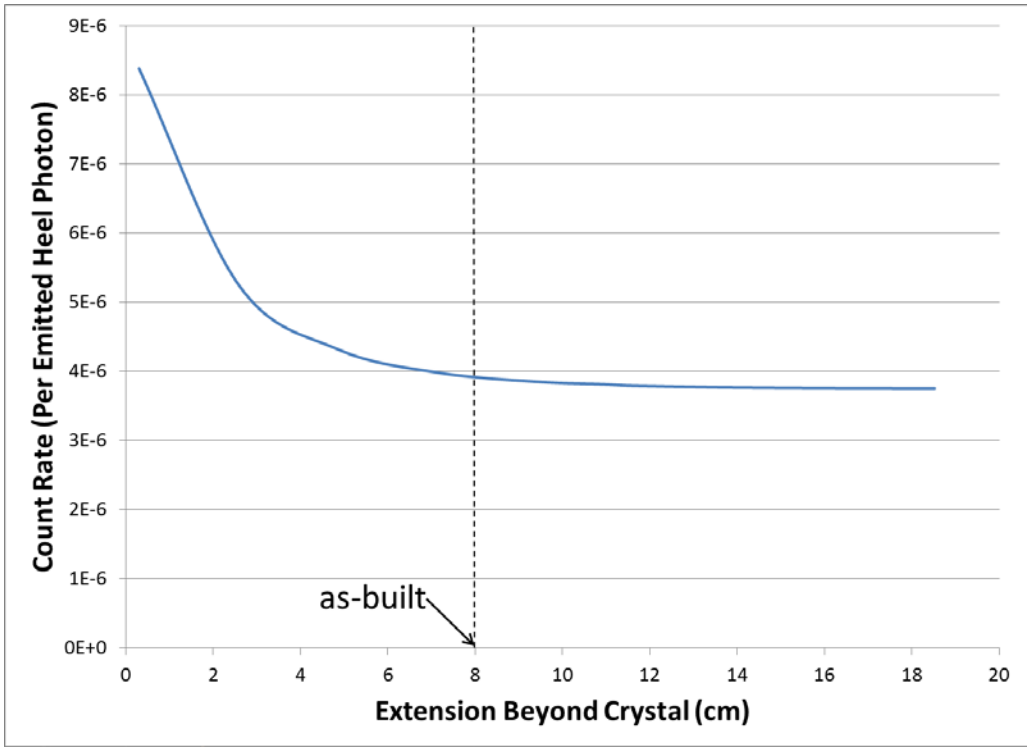

Figure 16. Count rate versus tungsten collimator length in terms of extension beyond the LaBr crystal.

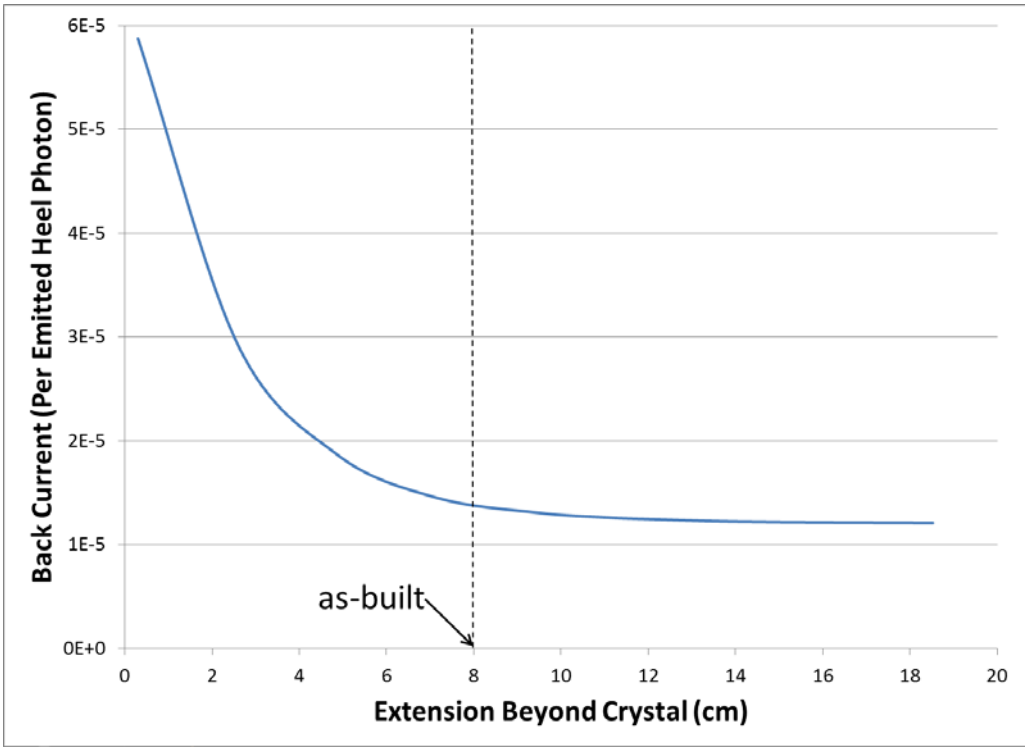

Figure 17. Photon current entering the Phase II LaBr crystal across the surface connected to the PMT.

3.2 Description of As-Built LaBr Gamma-ray Module Prototypes

As described in the previous sections, the as-built prototype LaBr-based gamma-ray module for UCVS Phase II consists of radiological design features informed by the radiation transport modeling study. The as-built gamma-ray module consists of the following noteworthy features:

- Compact, side-looking design that can be deployed in a clamshell configuration below the cylinder, which provides flexibility and a reduced form factor for the UCVS Phase II platforms, compared to the Phase I HEVA module design;
- Cylindrical tungsten shielding (machinable tungsten alloy, 18.5 g/cc) designed to reduce the scatter from the cylinder being assayed and nearby cylinders that can degrade the precision of the 186-keV ROI used in the enrichment meter method;
- Removable tungsten inserts that allow for varying the aperture opening (0 to 4-cm diameter) and thereby providing flexibility in managing count rates under the different deployment geometries envisioned for the stand-alone and modular configurations envisioned for the integrated UCVS Phase II platforms;
- Liquid-tight module housing including vents for pressure stabilization and cooling;
- Single-cable operation.

The fully assembled detector module is Ø10.2 cm × 36.8 cm and weighs 12.5 kg. The following set of figures depicts various parts of the as-built prototype LaBr gamma-ray module. Note that the module design would need to be modified somewhat in order to accommodate commercially available CZT spectrometers.

The aperture plug is designed for experimentally determining the shielding performance of the tungsten alloy. A set of gamma-ray spectra measured with the aperture fully open (4 cm) vs. fully closed (0 cm) will assist in benchmarking the MCNP model against experiment.

Self-activity in LaBr can be a concern for some applications, particularly those in which relatively weak signals from the sample (e.g., heavily shielded caves on environmental samples) can be significantly obscured by emissions from electron capture and beta decay in ^{138}La. For example, the intrinsic activity in a LaBr crystal of the size used in the prototype modules (i.e., 3.8-cm right circular cylinder) will produce approximately 6 cps in the energy range between 140 keV and 240 keV—the ROI important to the enrichment-meter method (Quarati 2012). For a UF_6 cylinder verification scenario, this self-activity signal from LaBr is anticipated to be a nonfactor for several reasons, including: 1) the self-activity signal is very small compared to even the lowest-enrichment cylinders (i.e., a perfectly clean DU cylinder presents over 600 cps in the 140-240 keV range for this prototype module design, and count rates from heeled cylinders will be even higher); 2) the self-activity signal is constant in time and therefore, a constant offset that can be subtracted using even the simplest of background-removal algorithms, and 3) the signal is a continuum that is largely removed by the peak-extraction algorithms employed in UCVS (e.g., SWC or NaIGEM).

Figure 18. Tungsten collimator with inserts of varying aperture diameter: 2 cm, 3 cm, 4 cm, and full plug (top left), detector assembly (top right), and dual liquid-tight air vents along with sealed Power over Ethernet (PoE) port equipped with collimator aligning notch (bottom).

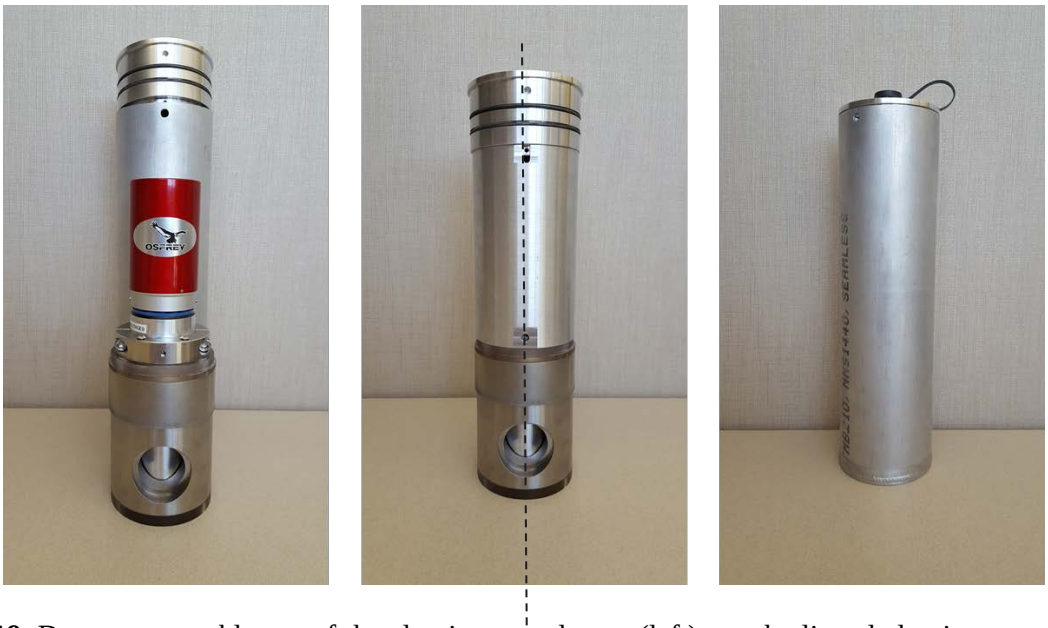

Figure 19. Detector assembly out of the aluminum enclosure (left), notch-aligned aluminum spacer with dual O-ring top-cap (center), and fully assembled detector module (right).

3.3 Laboratory Testing of Gamma-ray Module Prototypes

Laboratory measurements were performed to provide initial characterization and calibration of a prototype LaBr-based gamma-ray module. Characterization and refinement of the Osprey parameters must be performed over a representative range of input count rates. For the cylinder assay scenario, the HEVA input count rate can vary significantly between cylinders, not just because of varying enrichment levels but also because of the amount of uranium-bearing compounds and ^{238}U progeny on the bottom and walls of the cylinder, referred to as heels in this report.

3.3.1 Trapezoidal Filter Parameters: Rise-time and Flat-top time for LaBr

The Osprey employs a digital trapezoidal filter that allows the user to independently set the rise time (RT) and flat-top time (FT) according to the scintillator type and desired performance. Figure 20 depicts these timing parameters.

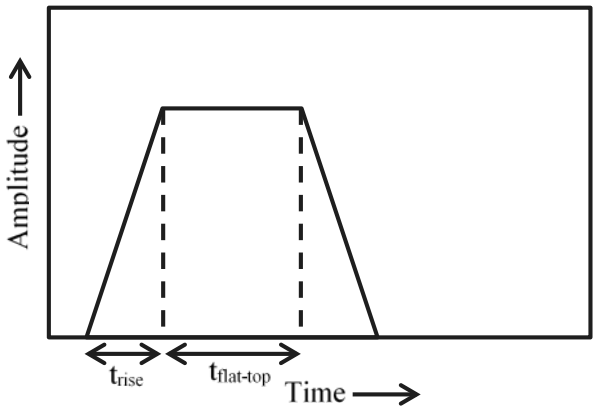

Figure 20. Digital pulse processing using a trapezoidal filter.

In theory, the RT of the trapezoidal filter should be long enough to allow collection of all scintillation light produced and therefore, maximize the signal to noise ratio. Generally speaking, RT values of approximately four times the scintillation decay constant (e.g., 0.23 μs for NaI) are generally recommended from the signal-to-noise perspective, but that must be balanced by practical throughput considerations since longer rise/fall times lead to more dead time.

The FT accounts for the degree of variability in the charge collection time of the detector. Partial and variable collection of the charge produced by the detector can significantly degrade energy resolution in some detector types. In general, FT values that are too short can lead to ballistic deficit effects on energy resolution, particularly for large semiconductor detectors. In the case of inorganic scintillators such as NaI or LaBr, each pulse is of the same length in time, without any dependence on the energy of the photon. Therefore, a single, relatively short FT value can be used.

In an Osprey, the total pulse shaping time, including the minimum spacing between pulses, required by the digital signal processor is $2.2 \times RT + 2 \times FT$. There is an obvious tradeoff between improved energy

resolution and minimized dead time. Longer pulse duration can increase the system dead time, which results in increased pulse pile up, degraded count rate performance and poorer resolution due to the broadening of the photo-peak (associated with the pile-up). For NaI and LaBr, the Canberra-recommended value for both RT and FT is approximately 1 μs. However, the scintillation decay time for LaBr (0.026 μs) is much shorter than that of NaI (0.23 μs) and therefore the RT/FT can be shortened in favor of higher throughput.

Using these Canberra recommendations as a starting point, PNNL performed a series of tests to provide empirical support for the RT and FT values to be used in the refined gamma-ray detection module. In order to determine a suitable setting for RT and FT, 30-second and 60-second real-time Cs-137 gamma-ray spectra were collected at following timing parameters: RT= [0.2, 0.4, 0.6, 0.8, 1.0, 1.2, 1.4, and 1.6] μs and FT = [0.3, 0.4, 0.5, 0.6, 0.7, 0.8, 0.9, 1.0, 1.1, and 1.2]. These measurements were conducted at low (~ 2.5 kcps), medium (~17 kcps), and high (~100 kcps) count rates. Figure 21, Figure 23, and Figure 25 show the relative full-width at half-maximum (FWHM) resolution at 662 keV for various RT and FT values at varying count rates. The error bars on the full-width at half-maximum (FWHM) resolution span ±0.1 % of the measured value (one sigma, statistical only) and are not shown for ease of readability. Figures 22, 24, and 26 show the dead-time for various RT and FT at varying count rate. These measurements were conducted using custom software that iteratively adjusts parameters and acquires data for fixed amounts of times. Table 2 lists all of the Osprey settings pertaining to these measurements.

Table 2. List of settings for RT/FT assessment of the LaBr-based module.

Parameter	Setting
HV (volts)	725
Total observed count rate (cps)	2.5 (low), 17 (medium), 100 (high)
Gain (Fine x Coarse)	1.0 x 1.0
Flat-top time (μs)	Variable
Rise-time (μs)	Variable
PUR Guard Time interval	2.2x
LTC	On
BLR mode	Auto
Fdisc setting	Auto
Fdisc shaping	Normal

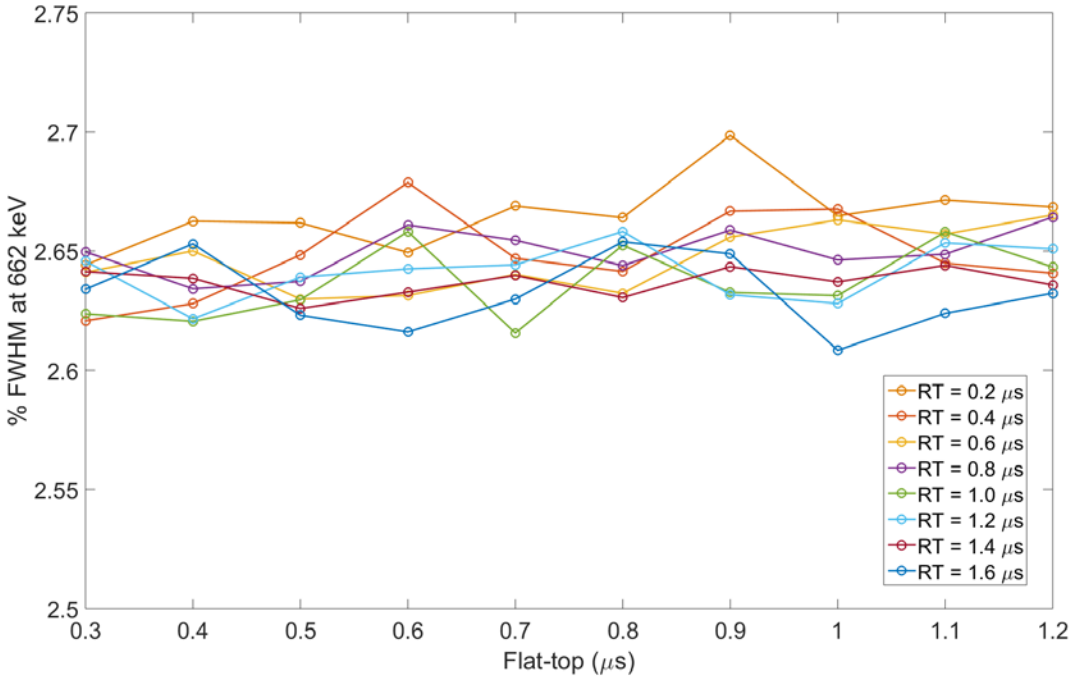

Figure 21. Relative FWHM as a function of RT and FT at low count rates.

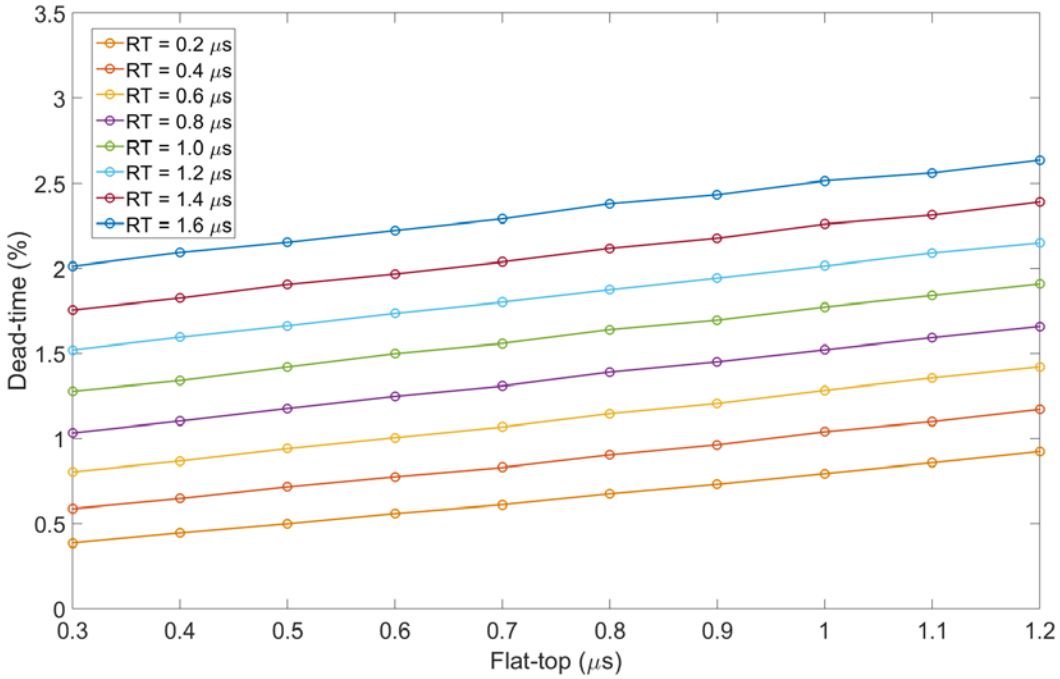

Figure 22. Dead-time as a function of RT and FT at low count rates.

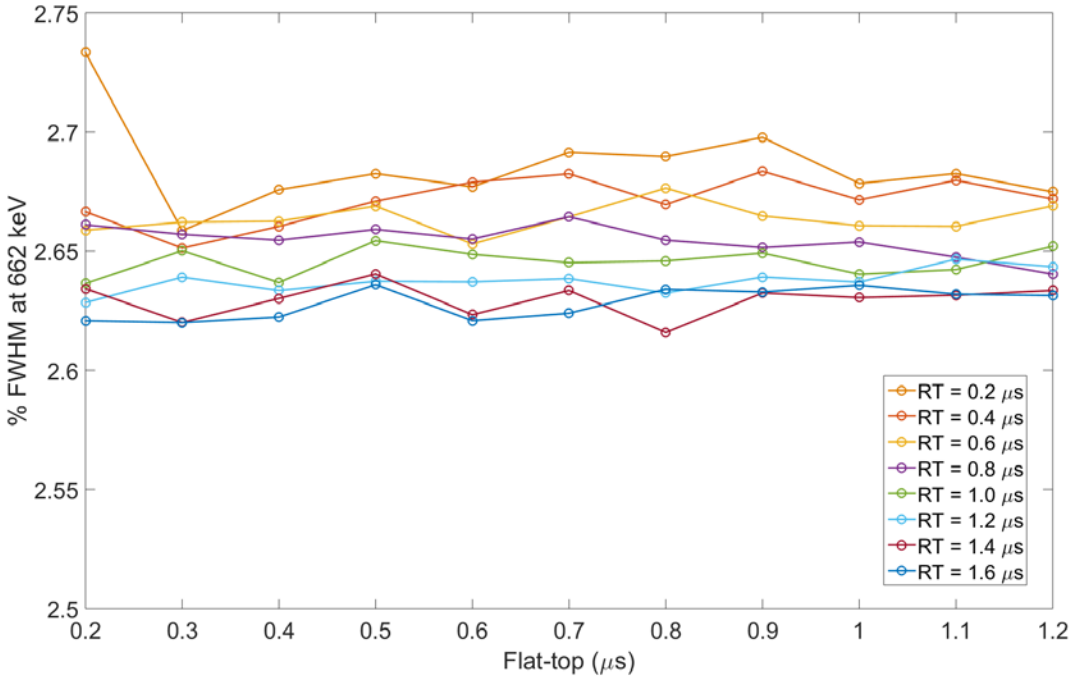

Figure 23. Relative FWHM as a function of RT and FT at medium count rates.

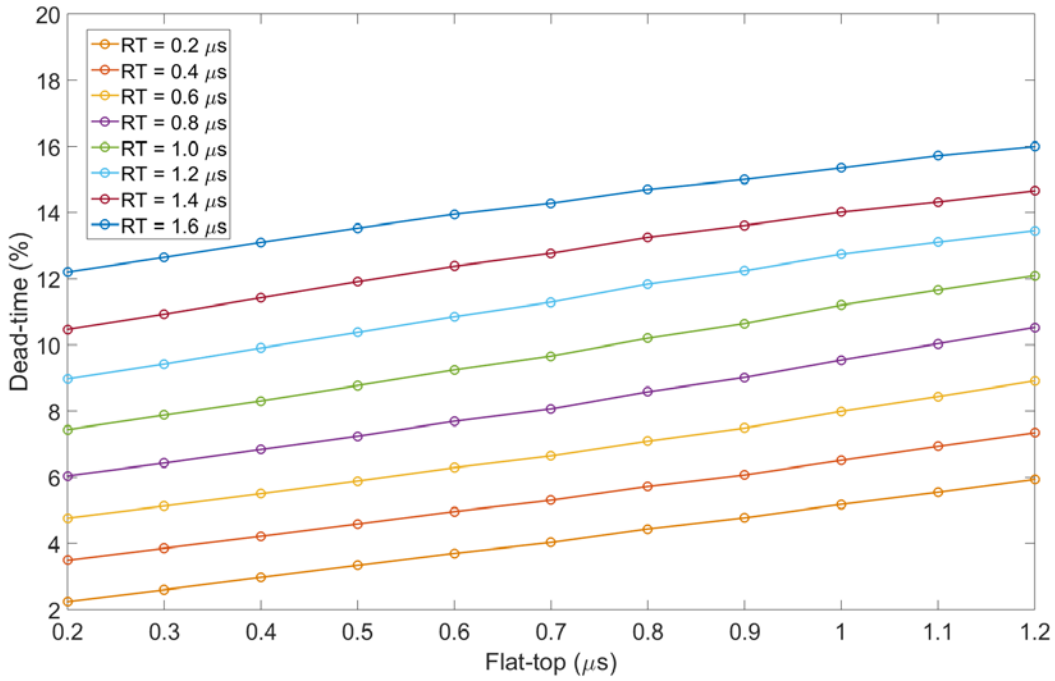

Figure 24. Dead-time as a function of RT and FT at medium count rates.

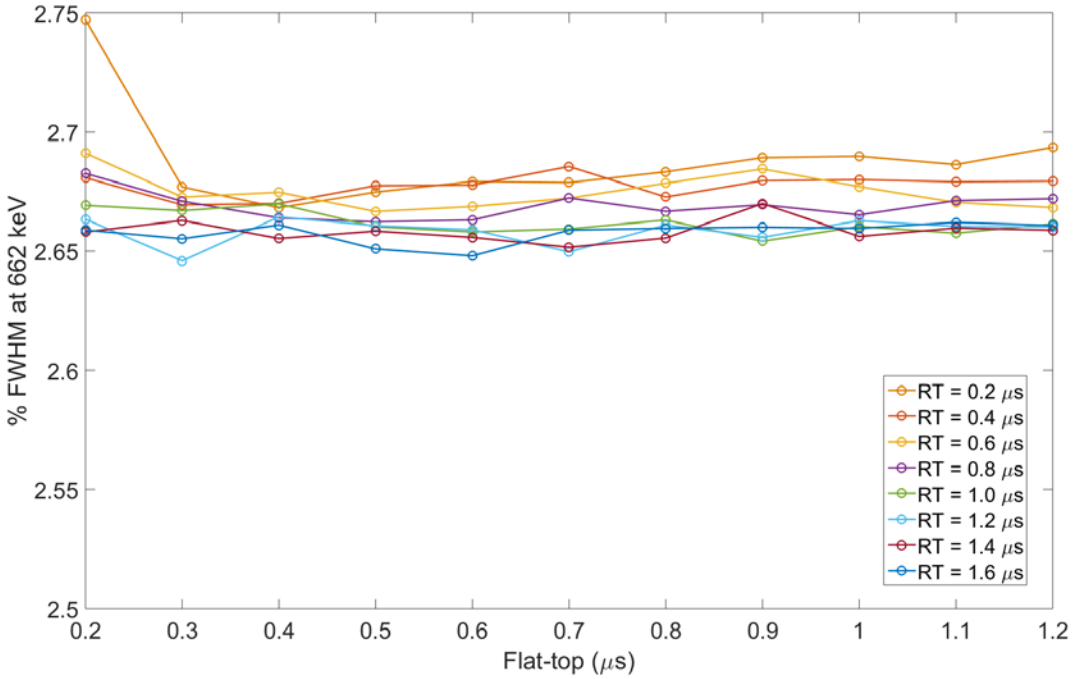

Figure 25. Relative FWHM as a function of RT and FT at high count rates.

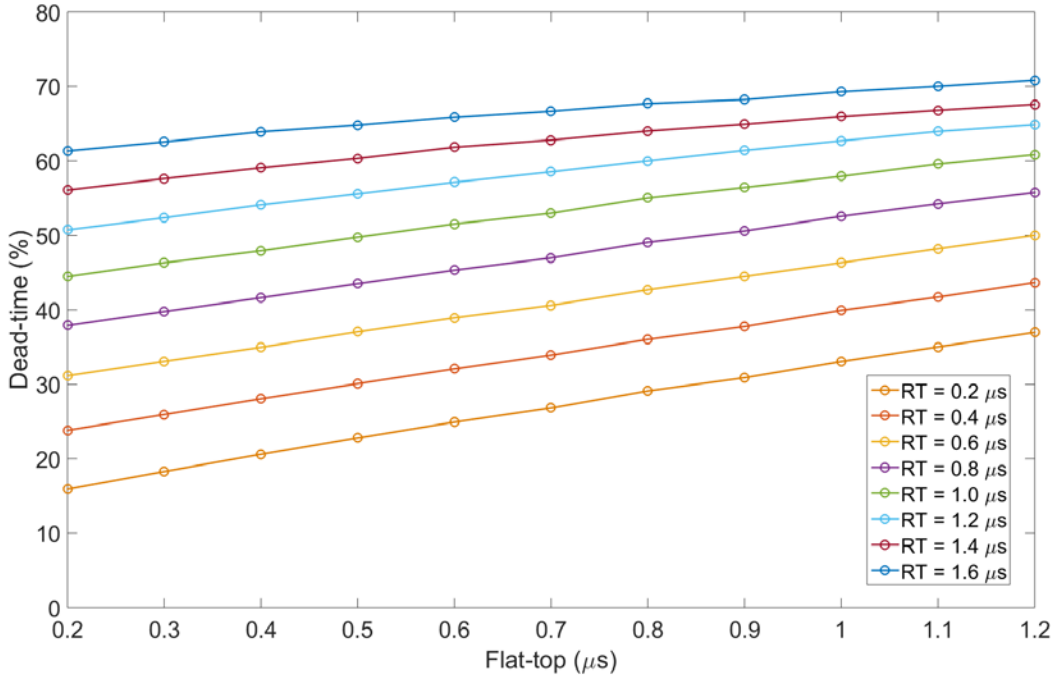

Figure 26. Dead-time as a function of RT and FT at high count rates.

Theory predicts that the highest achievable energy resolution can be attained by setting the shaping times longer to allow for full charge collection. However, longer shaping times can produce higher pile-up event rates, thus reducing the effective throughput of the system and often, degrading the absolute count-rate precision—a key factor in enrichment-meter measurements (Zalavadia 2016). Therefore, an appropriate balance must be struck between the throughput and energy resolution. Figure 21, Figure 23, and Figure 25 indicate that the relative FWHM at 662 keV remain constant between 2.6 and 2.8 percent for a relatively wide range of count rate, RT, and FT. Figure 23 and Figure 25 indicate that RT and FT of 0.2 µs leads to degraded energy resolution at medium and high count rates—whether this is due to insufficient charge collection, issues with the Osprey at the low end of its parameter range, or some combination thereof is not clear. Figure 22, Figure 24, and Figure 26 indicate that the dead-time increases linearly with increase in total pulse shaping time. It is therefore desired to keep the RT and FT (and thus the total shaping time) as low as possible without compromising on energy resolution. For the purposes of UCVS Phase II settings, these results indicate that any RT and FT value above 0.2 µs will yield consistent performance for energy resolution of approximately 2.7% FWHM for count rates at least to approximately 100 kcps, for the tested gamma-ray detector module. Note that the best practically achievable energy resolution, i.e. relative FWHM at 662 keV, for LaBr is between 2.6 and 3 percent. This particular UCVS Phase II detector module is operating near the most desirable end of that range. Given the above findings, any combination of RT = [0.4, 0.6] µs and FT = [0.3, 0.4] µs is a suitable setting for a wide range of input count rate.

3.3.2 Energy Resolution Characterization for LaBr Module

Operating scintillator-based detection systems at proper high voltage on the photomultiplier is important to achieving stable and optimum performance. Figure 27 shows the dependence of energy resolution (relative FWHM) on detector operating voltage for the Osprey-based LaBr module under test (photomultiplier tube is R6231-01 from Hamamatsu operating with positive-polarity high voltage). The energy resolution improves as charge multiplication increases at higher voltage. As noted earlier, the best energy resolution for LaBr at 662 keV is between 2.6 and 3% at a nominal operating voltage of 725 volts. Figure 27 indicates that an operating voltage of 625 volts and above yields resolution better than 3%, and that improvements in energy resolution diminish above ~750 volts. For the as-tested LaBr prototype modules, PNNL recommends a high voltage setting between 725 and 800 volts.

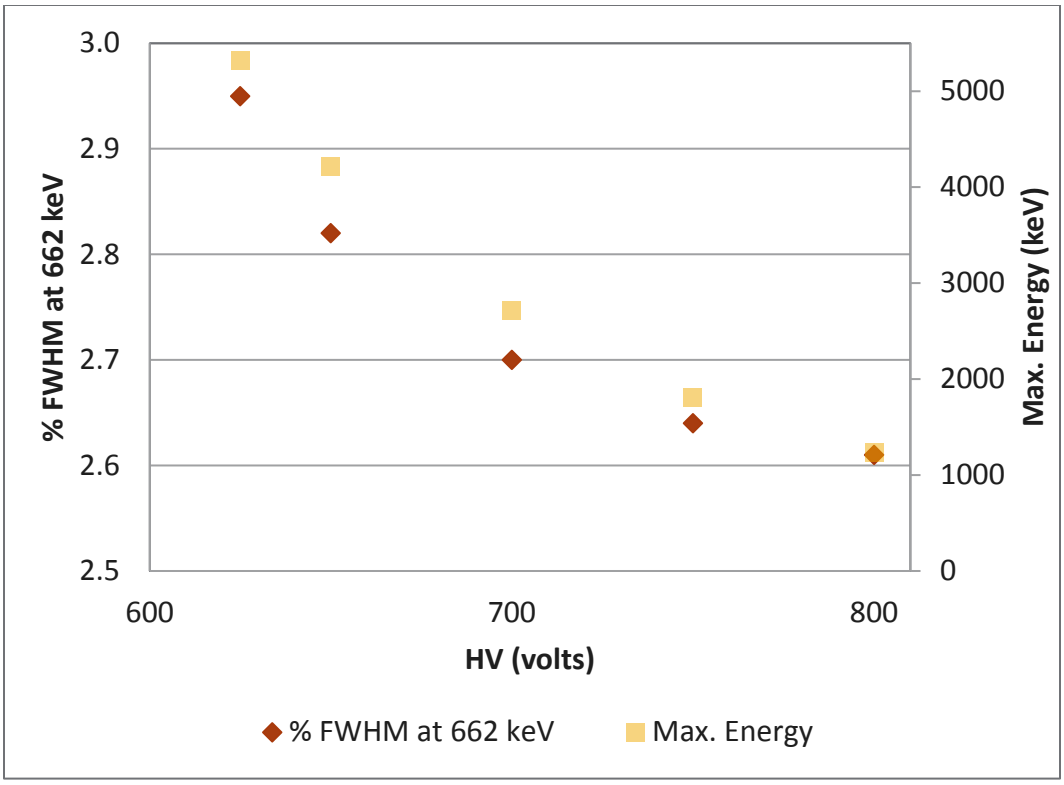

Figure 27. Relative FWHM at 662 keV as a function of operating voltage.

Figure 28 and Figure 29 shows the absolute and relative FWHM as a function of incident gamma-ray energy for the LaBr module under test, using an operating voltage of 750 volts, RT of 0.4 μs and FT of 0.3 μs. The fit to the absolute FWHM data in Figure 28 was obtained using the following relationship: $FWHM = a + b\sqrt{E + cE^2}$. The values of the fitting parameter a, b, c were found to be 0.00162, 0.019 and 0.0552, respectively. Vertical dashed lines are shown in these figures at 186 keV, the energy of primary interest in the enrichment-meter verification scenario. At that energy, the expected FWHM energy resolution is approximately 10 keV (6% relative).

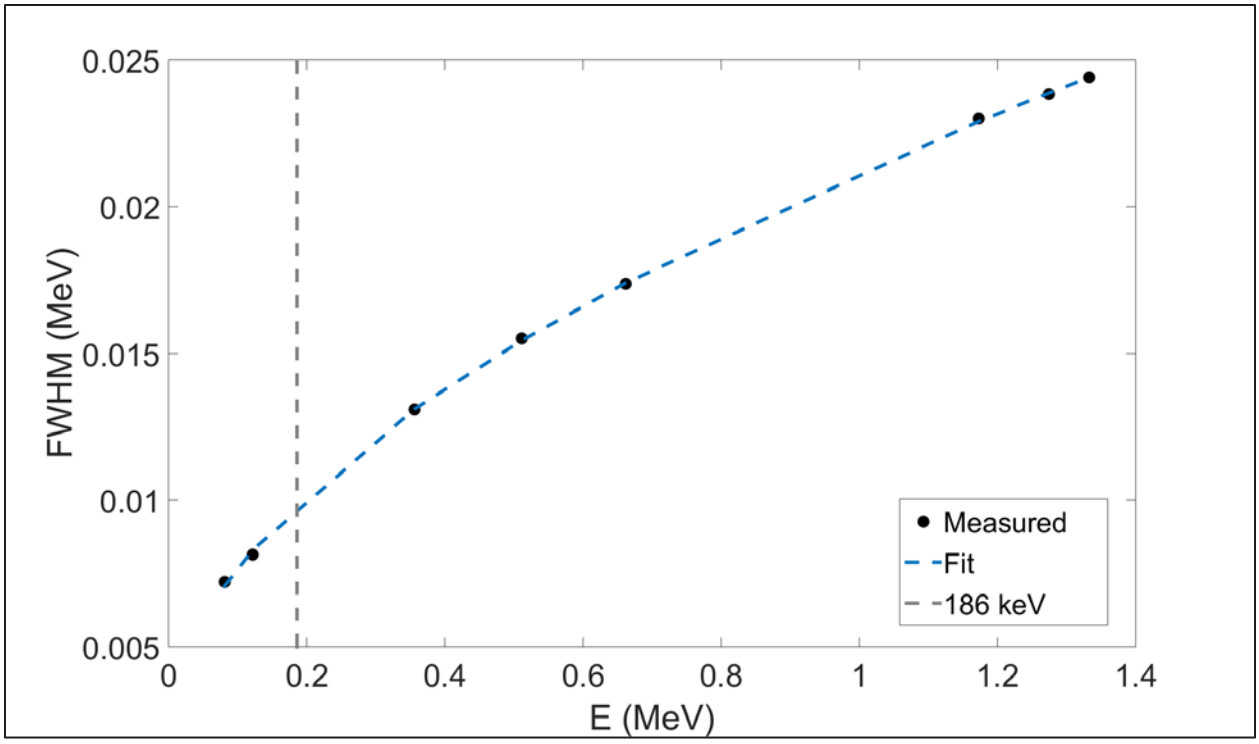

Figure 28. FWHM as a function of incident gamma-ray energy.

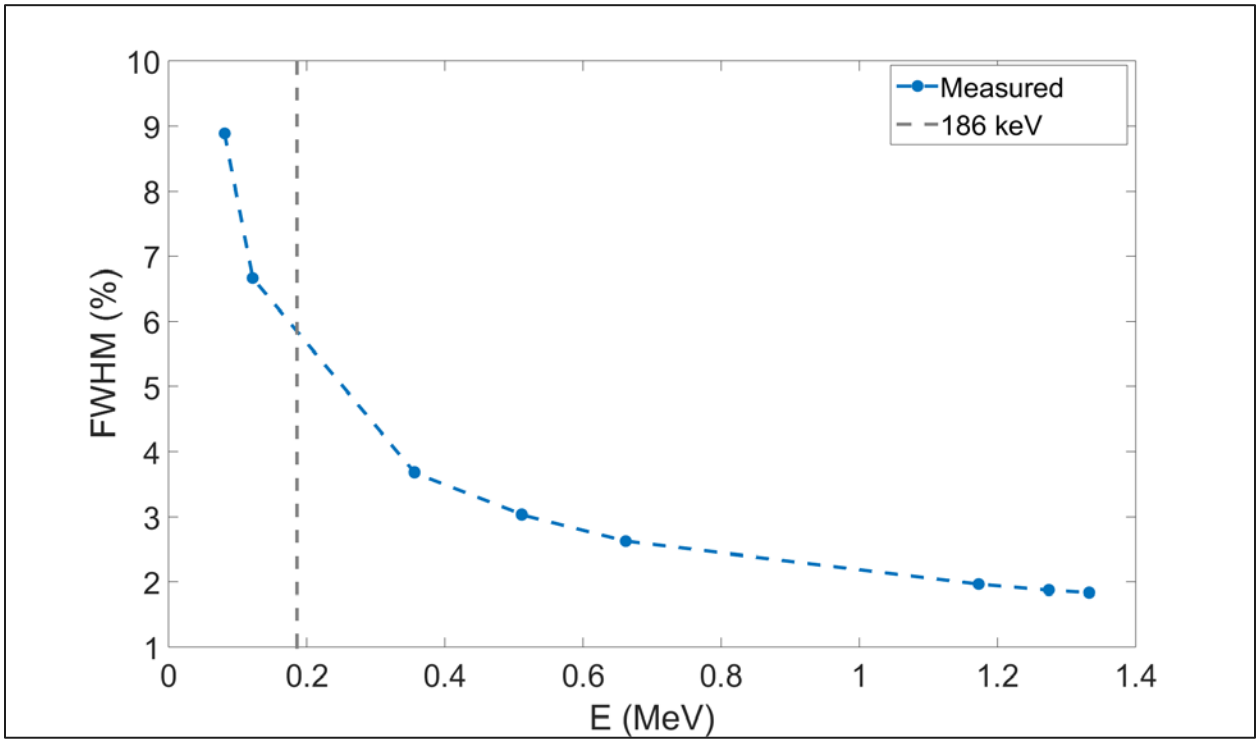

Figure 29. Relative FWHM as a function of incident gamma-ray energy.

3.3.3 LaBr vs. Sodium Iodide Resolution Comparison

A key motivation for considering LaBr instead of NaI in the Phase II gamma-ray modules is the higher energy resolution of LaBr and the presumed improvements in enrichment-meter performance that spawn from that improved energy resolution. Figure 30 shows a comparison of energy resolution for NaI and LaBr modules tested by PNNL. The energy resolution at 662 keV for LaBr is approximately three times better than that of NaI. However, at the primary energy of interest in UF_6 assay, 186 keV, the LaBr energy resolution is only two times better than that of NaI. This behavior is well-documented in these two scintillator types and is primarily due to the higher degree of nonlinearity in scintillation-light production in LaBr, as compared to NaI.

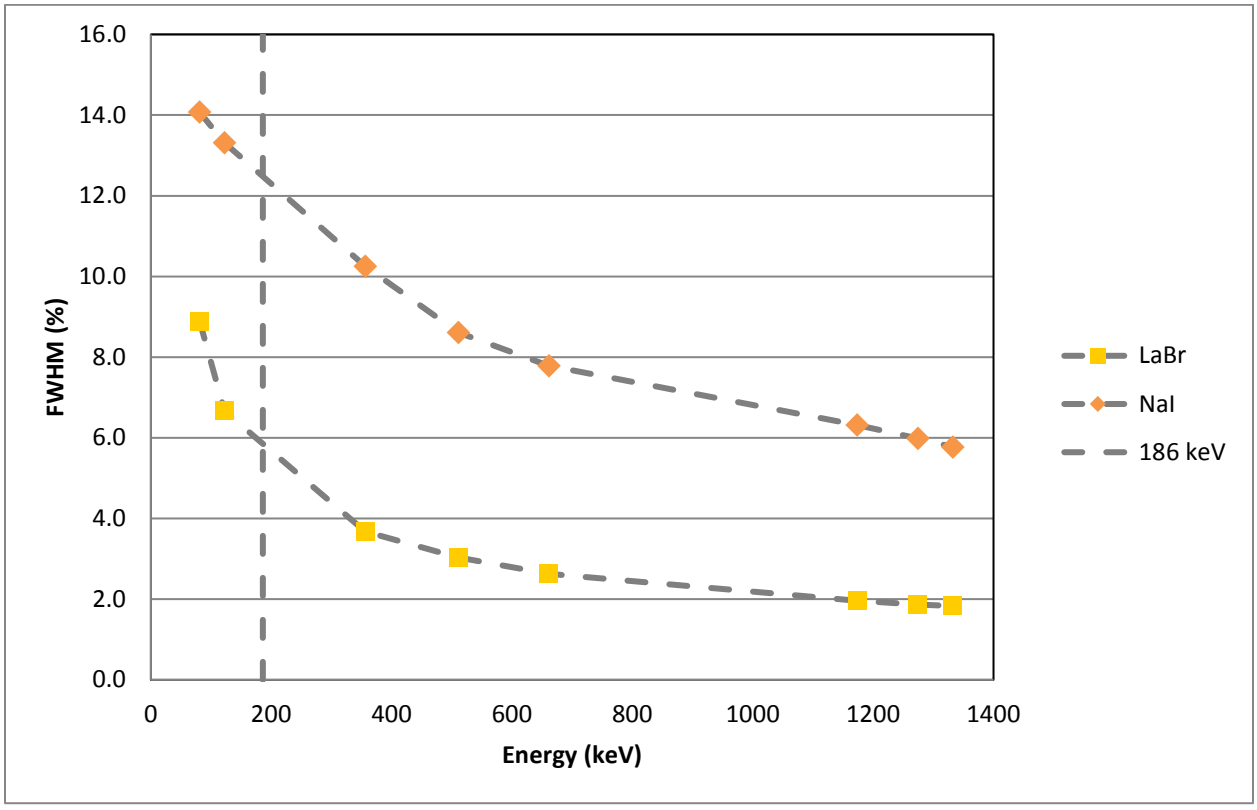

Figure 30. Comparison of relative FWHM between NaI and LaBr.

4.0 Comparative Evaluation of Gamma-ray Spectrometer Performance for Enrichment-Meter Verification Method

A key finding from UCVS Phase I was the need for improvements in the performance of the enrichment-meter method for the unattended cylinder verification scenario. Hardware and software adaptations are needed to more faithfully deconvolve the bremsstrahlung and down-scatter from ^{234m}Pa emissions in the bulk UF_6 and wall deposits.

As discussed previously, the Phase I gamma-ray modules were based on NaI for several reasons, including the HEVA method's reliance on the iodine in NaI for much of the neutron-to-gamma conversion process in the non-traditional neutron signal. Since the UCVS Phase II gamma-ray module will be purely a gamma-ray spectrometer (i.e., neutron detection will be accomplished using ^{3}He tubes), other room-temperature, cost-effective, commercially available gamma-ray spectrometer options can be considered. The two obvious candidates are LaBr and CZT and both have been considered in this comparative evaluation of spectrometer performance in the UCVS scenario.

While enrichments up to 4.95wt% were considered in this study, the emphasis is on finding improvements in performance, relative to the Phase I NaI spectrometers, for NU and DU cylinders with heavy wall deposits. As in nearly all gamma-ray spectrometry applications, enrichment-meter performance depends largely on a combination of energy resolution and absolute collection efficiency for the 186-keV signature emanating from the cylinder.

This section describes modeling and analysis steps taken by PNNL to support the adaptation and enhancement of the enrichment-meter method in Phase II, including:

- Use of MCNP to generate a library of simulated spectra for NaI (HEVA and $UCVS_{EM}$ configuration), LaBr (HEVA and $UCVS_{EM}$ configuration) and CZT ($UCVS_{EM}$ configuration only), benchmarked using Phase I NaI data in the HEVA configuration;
- Using these synthetic spectra sets and PNNL's Square Wave Convolute (SWC) algorithm, comparative analysis of predicted enrichment-meter performance as a function of detector type, level of heel (wall deposit), and cylinder enrichment;
- Purchase and initial evaluation of the IAEA's version of NaIGEM (as used in attended cylinder verification) using Phase I field data from a HEVA-NaI, and comparison to the performance achieved using the SWC algorithm for the same cylinder population;

4.1 MCNP-generated Synthetic Gamma-ray Spectra

LaBr and CZT-based synthetic spectra were generated, assuming the as-built Phase II gamma-ray module prototype design shown in Figure 31. A 3-cm aperture diameter was assumed for both detector types, for simplicity in comparison, despite the somewhat smaller dimension of the CZT crystal. The CZT crystal, with a volume of 1500 mm^3 (1.5 cm^3), was modeled as a quasi-hemispherical (rectangular parallelepiped) crystal with dimensions of 1.44 cm by 1.44 cm by 0.72 cm thick. Synthetic spectra were also generated for the HEVA-NaI from Phase I, for the sake of comparison and quantitative connections to analysis of Phase I field data. These synthetic spectra were generated using the modeling methods described in previous sections for a perfectly clean cylinder (see Figure 6, all bulk UF_6), a cylinder with a mid-range heel level,

and a cylinder with a very high heel level as calculated for cylinder CYL3 (see Figure 7). The UF_6 material for each of these cylinders was varied across the following four ^{235}U enrichments, in wt%: 0.253 (DU), 0.710 (NU), 2.53, and 4.95. Therefore, 36 spectra (3 detectors × 3 heels × 4 enrichments) were generated, in total.

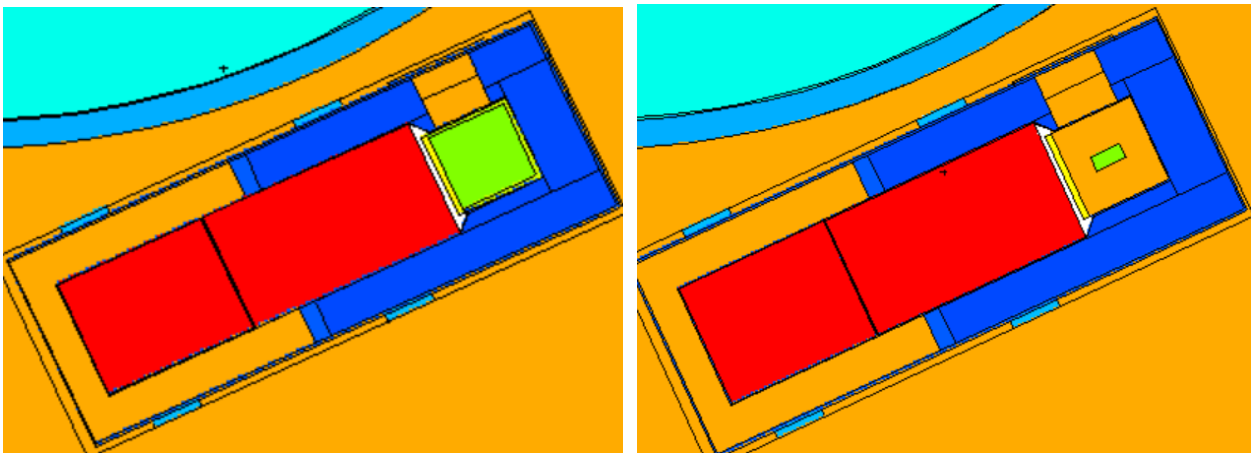

Figure 31. LaBr (Left) and CZT (Right) crystals in a nominal Phase II collimator design. The detector crystal in each figure is shown in fluorescent green centered within the collimator aperture.

The simulated spectra are shown for HEVA-2-NaI in Figure 32 and Figure 33, for Phase II LaBr in Figure 34 and Figure 35, and for Phase II CZT in Figure 36 and Figure 37. The Phase II LaBr spectra shown were generated using a resolution versus energy curve measured from PNNL's LaBr detector characterized in the previous section, and is assumed to be representative of the additional LaBr spectrometers that would be deployed in a Phase II prototype. Spectra from each detector are shown in linear scale, for energies up to just above the 1001 keV photopeak from ^{234m}Pa, since this is the region of the spectrum used to determine relative enrichment (though in field operation, the energy range will likely extend to approximately 3 MeV to ensure detection of the 2614-keV line from ^{232}U in reactor-recycle uranium). All of the simulated spectra were produced by convolving the un-broadened pulse-height MCNP tally with a Gaussian function with the appropriate resolution as a function of energy. Note that the simulated spectra shown in the figures below were based on MCNP calculations run long enough to achieve less than 1% statistical uncertainty in the tally of full-energy 186-keV events in each detector types. For the NaI, LaBr and CZT detectors, this translates to assumed assay times of approximately 3.9 hours, 15.5 hours and 341 days, respectively, which is well beyond the occupancy durations of UCVS, but provides the statistical precision needed to discern weaker spectral features, even for a CZT detector with low collection efficiency.

As expected, the large, 7.62 cm by 7.62 cm (3" by 3") HEVA-2-NaI module yielded the highest gross count rate across the three types of detectors, but the poorest energy resolution. CZT, on the other hand, has a much superior energy resolution relative to NaI and LaBr, but due to its small crystal size, the collected count rate is much lower, making it more difficult to obtain sufficient statistical precision in the relatively short occupancy times (less than 5 minutes) envisioned for the UCVS verification scenario. For example, for the simulated, clean, 4.95 wt% ^{235}U cylinder, the estimated overall gross count rate for a single 1.5 cm^3 CZT detector in the Phase II collimator was 680 cps, compared with 3.9 kcps for the Phase II LaBr and 11.5 kcps for the HEVA-2-NaI.

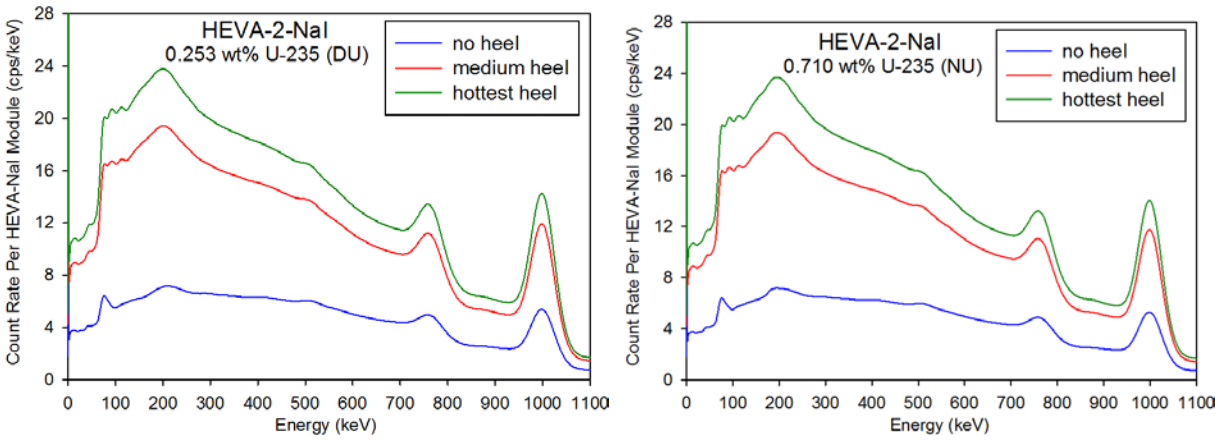

Figure 32. HEVA-2-NaI synthetic spectra for Left: a DU cylinder and Right: an NU cylinder, both with heels of varying radioactivity.

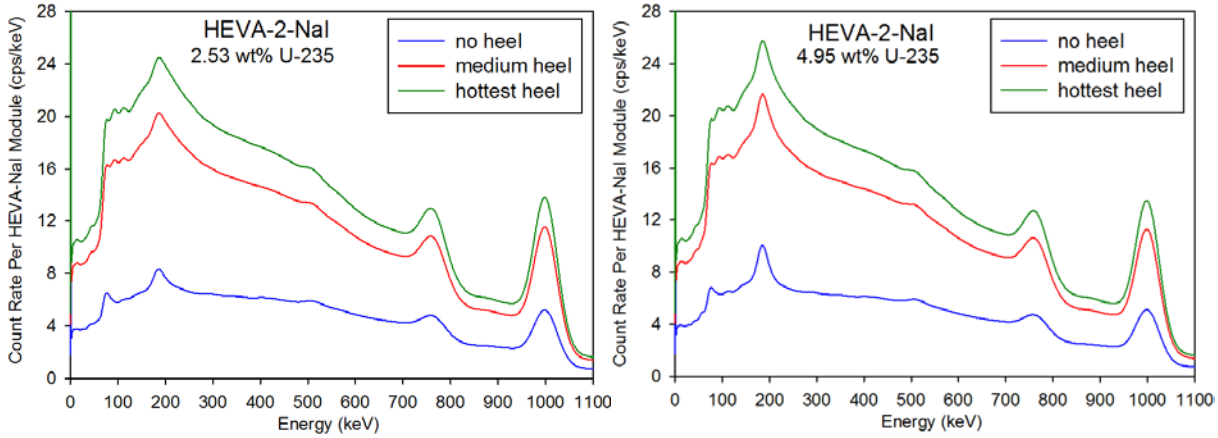

Figure 33. HEVA-2-NaI synthetic spectra for Left: a 2.53 wt% ^{235}U cylinder and Right: a 4.95 wt% ^{235}U cylinder, both with heels of varying radioactivity.

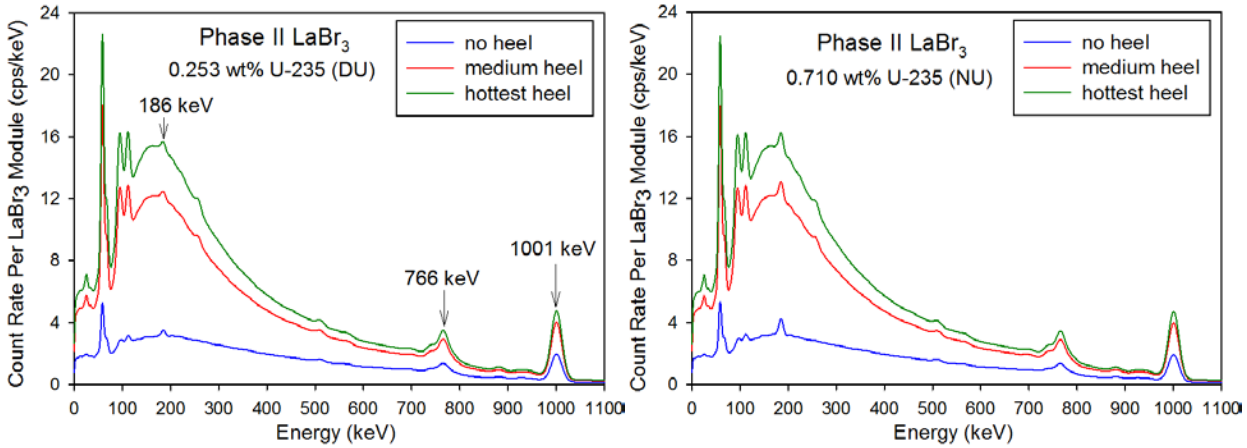

Figure 34. Phase II LaBr synthetic spectra for Left: a DU cylinder and Right: an NU cylinder, both with heels of varying radioactivity.

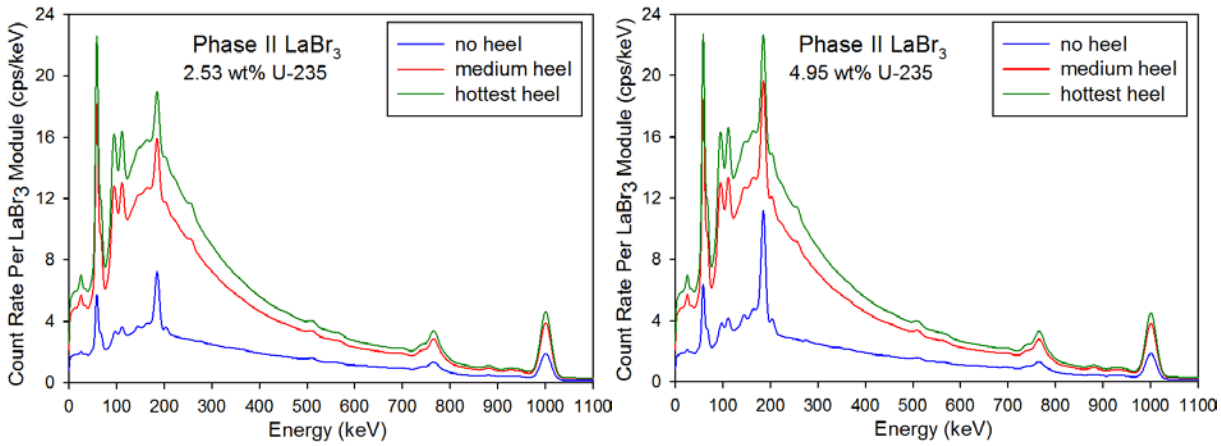

Figure 35. Phase II LaBr synthetic spectra for Left: a 2.53 wt% ^{235}U cylinder and Right: a 4.95 wt% ^{235}U cylinder, both with heels of varying radioactivity.

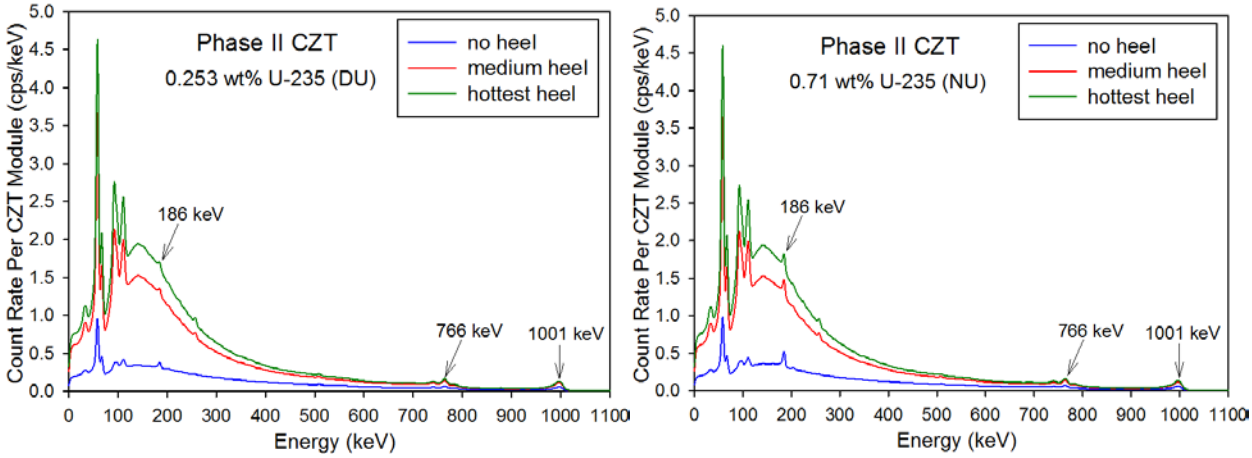

Figure 36. Phase II CZT synthetic spectra for Left: a DU cylinder and Right: an NU cylinder, both with heels of varying radioactivity.

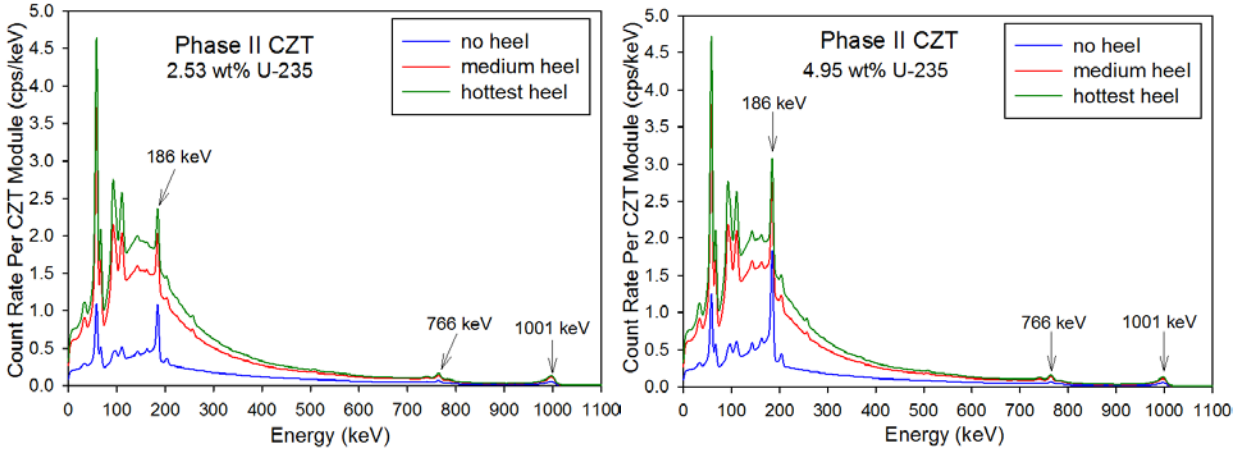

Figure 37. Phase II CZT synthetic spectra for Left: a 2.53 wt% ^{235}U cylinder and Right: a 4.95 wt% ^{235}U cylinder, both with heels of varying radioactivity.

4.2 Comparative Evaluation using SWC Analysis Algorithm

Utilizing the synthetic MCNP spectra described previously for representative UCVS verification scenarios, a comparative evaluation of spectrometer performance was performed using the Square Wave Convolute (SWC) methodology developed and exercised by PNNL in multiple field trials since approximately 2008 (Smith 2014)(Smith 2015)(Smith 2016). All previous SWC analysis was performed on NaI spectra but in this evaluation, the SWC algorithm was applied to all three detector types: NaI, LaBr and CZT. Relevant factors that could impact the relative performance of the three detector types are (1) collection efficiency, as manifested in the count rate in channels of interest as a result of module geometry changes or occupancy time constraints, (2) different continuum characteristics as a result of differing detector energy resolution, and (3) uncertainty in energy calibration leading to peak misidentification. In the following sections, the basic SWC algorithm and its properties are reviewed before discussing the relative performance gains of the detector/collimator configurations in relation to enrichment prediction. Potential strengths and weaknesses for practical implementation in an unattended cylinder verification scenario are also discussed.

In the discussion that follows, the nominal FWHM of the 186-keV peak for each detector was used to normalize the SWC window width to allow comparison of performance as a function of FWHM, rather than keV. The normalization values for each detector type are given in Table 3.

Table 3. Nominal FWHM values, at 186 keV, for the three detectors included in the comparative study.

Detector	FWHM (keV)
NaI	23 keV
LaBr	9 keV
CZT	6 keV

This investigation compares three specific UCVS gamma-ray module variants described previously but summarized here:

1. HEVA-NaI: As deployed in Phase I, this module design includes a polyethylene/iron collimator that is necessary for the HEVA indirect neutron signature, but results in higher down-scatter continuum effects that tend to degrade performance for the SWC enrichment-meter method.
2. Phase II LaBr: Nominal Phase II design with a side-looking configuration with heavy tungsten collimator that reduces down-scatter continuum. Energy resolution parameters are consistent with the prototype module developed and lab-tested by PNNL, described earlier.
3. Phase II CZT: Nominal Phase II design based on a relatively large commercially available quasi-hemispherical crystal (i.e., Ritec's microSpec 1500) and the same tungsten collimator used in the LaBr module design.

4.2.1 Square Wave Convolute Methodology

The ultimate goal of the enrichment-meter analysis is to predict the enrichment of a given cylinder, which is tied to the net counts in the 185.7 keV peak. Therefore, any proposed analysis must be able to handle the separation of background continuum and the net 186-keV signal in the presence of statistical noise. In essence, the Square Wave Convolute (SWC) method is a weighted average of a subset of channels in a

spectrum with the goal of removing a linear background contribution as well as smoothing noise to determine net counts under a peak. This can be viewed as a modification to classic numeric integration procedures like the trapezoidal rule. For any spectrum $f(x)$ where x is the channel, the SWC method determines that the net count rate in the peak is approximated by:

$$SWC(x) = \sum_{i=-n}^{n} f(x+i)g(i)$$

where the filtering wavelet $g(i)$ is defined to be

$$g(i) = w(i) - \frac{1}{2n+1}\sum_{i=-n}^{n} w(i)$$

and $w(i)$ is the discretized cosine square wave function with period $2n$.

Peaks that differ from statistical noise are defined to be local maxima of $SWC(x) > \tau$. There are two major parameters that can be adjusted to capture the peaks of interest – the size of the wavelet (the number of channels to use in our numeric integration scheme - n) and the peak height (the minimal number of counts above background to be designated as significant - τ). Optimal settings for both parameters are dependent on the width of the peak (i.e., energy resolution of the spectrometer), the proximity of other peaks to the primary peak of interest, and the amount of statistical noise present.

The value of n should be large enough to capture the entire peak width and smooth out the statistical noise without capturing any other peaks. Similarly, τ needs to be large enough to screen out statistical noise, but small enough to capture weak signals. In this study, a portion of the continuum where no significant peaks are present (from 250 keV to 400 keV) was utilized to quantify the amount of statistical variation in the SWC signal. The algorithm required that peaks have a net count rate exceeding three times this standard deviation, i.e. $\tau = 3\sigma$, in order to identify it as a detected peak. Decreasing this threshold is possible but will increase the likelihood that the 185.7 keV peak is incorrectly identified due to spurious statistical variation or when a precise energy calibration cannot be determined.

4.2.2 Performance Comparisons without Statistical Noise

In the first performance comparison, an infinitely converged measurement (no statistical noise) was assumed. Figure 38 and Figure 39 below are examples of the spectra for the 4.95% enrichment and 0.2% enrichment cylinders, for the three detector types. These high-precision spectra reveal a number of spectral features, e.g., the 145, 165 and 205 keV peaks in the case of LaBr and CZT that are not always evident in spectra from UCVS-like occupancy times—less than five minutes. They also depict how these weaker features are not visibly present at all in NaI and importantly, the HEVA-NaI design does not generate the tungsten x-rays that could prove important to robust unattended energy calibration in Phase II.

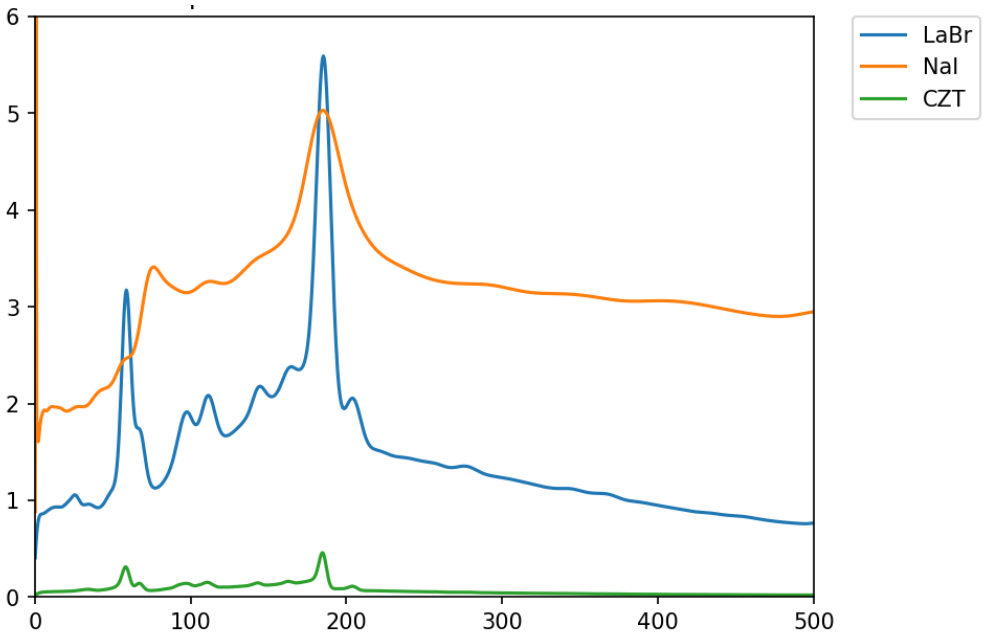

Figure 38. Example spectra for 4.95wt % cylinder for the HEVA-NaI, Phase II LaBr and Phase II CZT detectors.

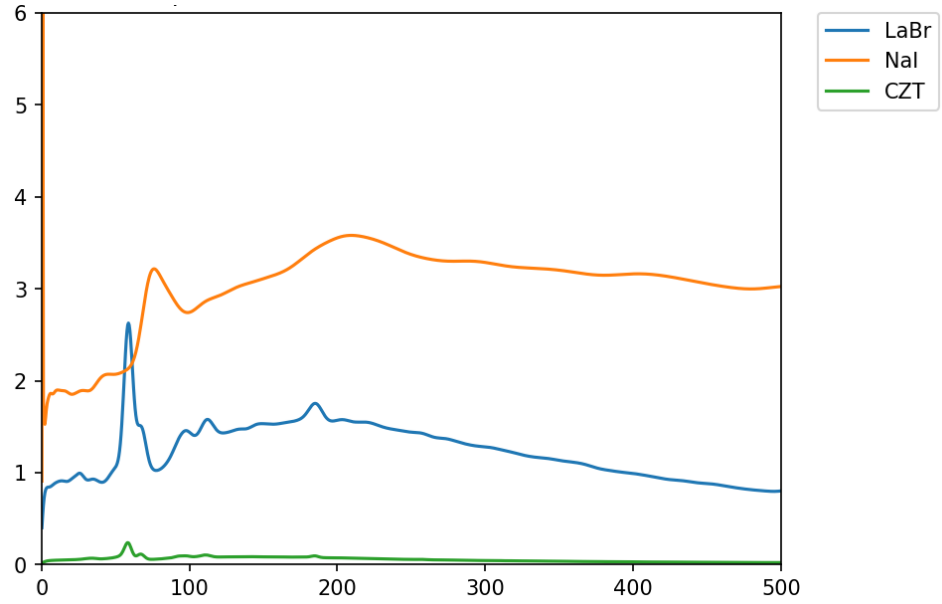

Figure 39. Example spectra for 0.25wt % cylinder for the HEVA-NaI, Phase II LaBr and Phase II CZT detectors. Note that the high down-scatter of the HEVA-NaI design, manifested as a hump peaked nearly 210 keV, largely obscures the weak 186-keV signature.

Enrichment-meter performance can be captured by examining the standard deviation of the relative error (RSD) in predicted versus actual enrichment. The RSD can be considered for two different slices of the data: 1) the RSD in predicted enrichment for each cylinder (averaging error over heel type), and 2) the RSD for each heel profile over all enrichments. As shown in the images below, the LaBr and CZT detectors

outperform the NaI detector regardless of the cylinder enrichment or heel type, under an infinite-measurement-time assumption. These figures also show that as the SWC window size is increased, and more peaks (i.e., beyond the 186 keV) are included in the moving average of the wavelet analysis, even the error rate for LaBr detectors begins to increase. Even under an infinite-time assumption, the hottest heels and lowest enrichments remain a challenge in terms of accurately predicting enrichments.

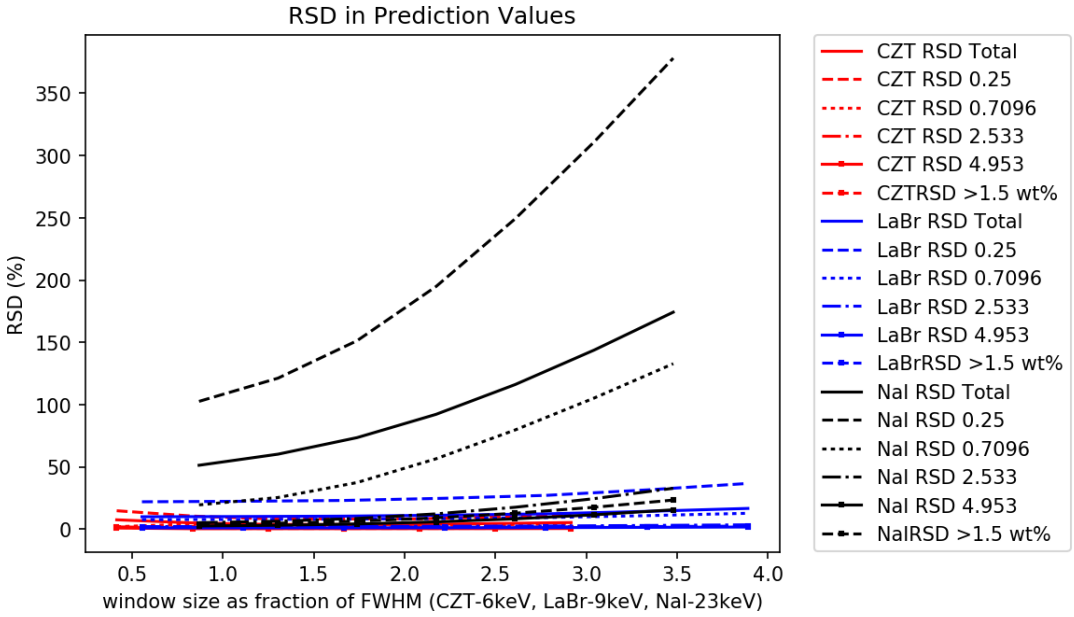

Figure 40. RSD binned by enrichment and detector.

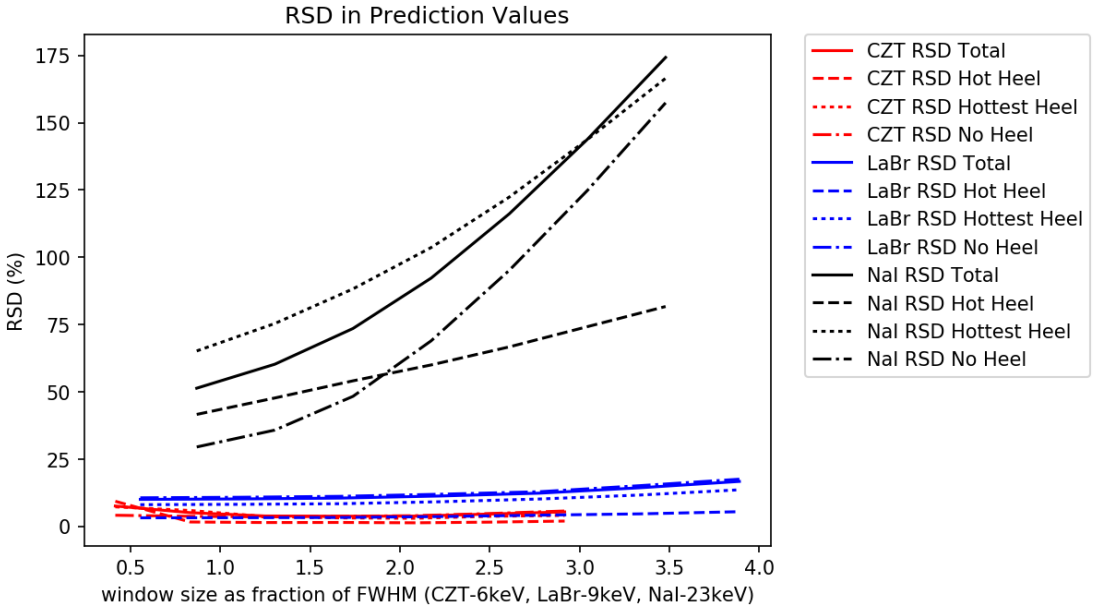

Figure 41. RSD binned by heel type and detector.

As shown in Figure 40, the prediction error does not differ significantly for the three detector types, at the higher enrichments of 2.5wt% and 4.95wt%. That is, under the infinite-time assumption the signal is large and clearly differentiable from the background continuum for all three detectors. But the performance difference between NaI and the two higher-resolution sensors is notable for the NU and DU cylinders of most interest in this study.

When RSD values are binned by heel intensity as in Figure 41, the results are generally consistent with intuition in that the RSD for the lower-heel cylinders are lower than for the hottest-heel cylinders. The exception to this trend is in the NaI curve for clean (i.e., no-heel) cylinders and window sizes greater than approximately 2.0 times the FWHM. There, the performance on the hot-heel cylinders is actually better than the no-heel cylinders. The reason for this non-intuitive behavior is that the simulated population of cylinders is biased toward higher heels (i.e., 8 of 12 spectra for each detector type have relatively high heel levels even though those cylinder types may be less common in real cylinder populations) and therefore the calibration process that relates net SWC signal to enrichment (via a least-squares fitting across all cylinders in the population) is "tuned" to extracting the 186-keV signal from very high continuum levels. For the clean, no-heel cylinders, this leads to a bias in the calibration process that grows as the SWC window grows. This trend is an artifact of the limited simulated cylinder population and emphasis on heavy heels, and would not affect larger, real-world populations in the same way.

4.2.3 Performance Comparisons with Statistical Noise

Building from the "infinite-assay-time" analysis described in the previous section, PNNL studied the predicted performance for the three detector types, using the SWC algorithms, for occupancy times expected to be representative of UCVS scenarios: 1 minute and 5 minutes. Algorithms were developed to add statistical noise, commensurate with occupancy duration, to the MCNP-generated spectra. Each channel in the infinite-time spectra provided the mean value of the counts in that energy region during the occupancy period, and a Poisson distribution was used on each channel to pull 100 different instances of each spectrum, renormalizing back to the counts per second frame. The figures below are example spectra from the 4.95% and 0.2% cylinders, for the two occupancy durations under study: 5 minutes and 1 minute. Clearly, the introduction of statistical noise negatively impacts the ability to visually identify the presence of the 185.7 keV peak in the DU cylinder for all detector types.

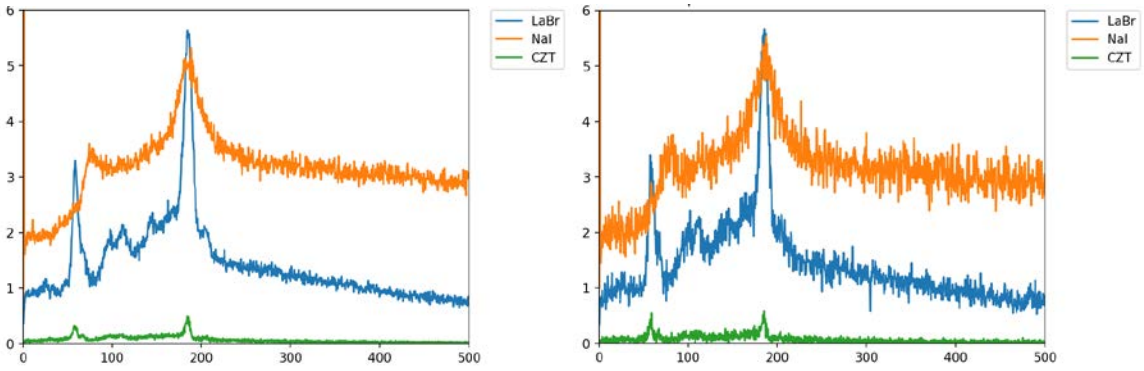

Figure 42. Example spectra for 4.95% enrichment with Poisson noise from a 5-minute collection (left) and 1-minute collection (right).

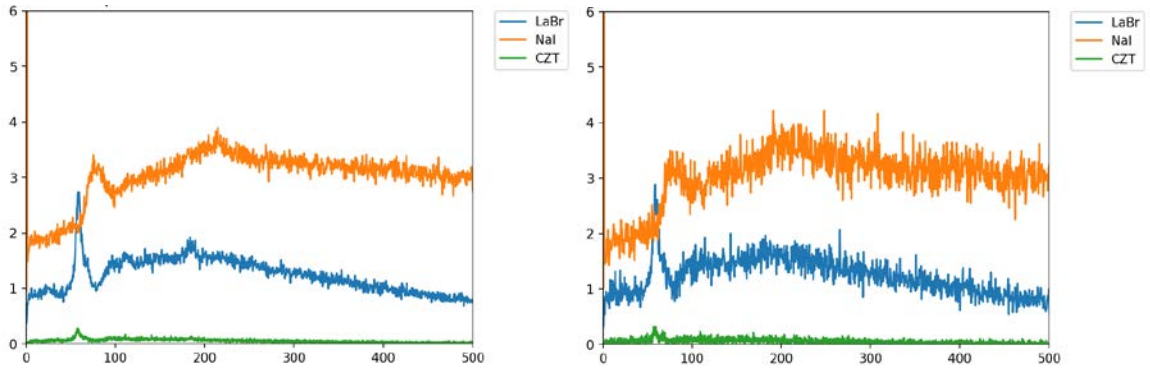

Figure 43. Example spectra for 0.25% enrichment with Poisson noise from a 5-minute collection (left) and 1-minute collection (right).

Examining the RSD results for these more-representative occupancy durations, some of the same trends seen in the infinite-time analysis are still present (i.e., the low enrichment cylinders and hottest heel types are driving the RSD to relatively high values). However, in contrast to the infinite-time measurement where the LaBr and CZT significantly outperformed NaI due to their higher energy resolution, the LaBr with the nominal Phase II collimator design consistently outperforms not only the NaI, but now also the CZT due to the low collection efficiency of the CZT spectrometer and "count-starved" nature of the spectra. This is particularly true for the 1-minute assay time on the DU and NU cylinders.

The statistical noise also introduces a somewhat different shape in the RSD trends as a function of FWHM multiplier. The quadratic shape of the RSD curves indicates that too narrow of an SWC window does not capture enough of the peak to make an accurate prediction of the enrichment due to higher statistical noise, but too wide of a window and other peaks begin to influence the noise levels. For the NaI detectors, it appears that an optimal window size is approximately 2 times the FWHM. The LaBr and CZT curves have a significantly flatter parabolic structure such that values between 2 and 3 times the FWHM provide approximately the same performance—a comforting result for unattended systems where energy resolution may fluctuate somewhat due to long-term temperature variations in the deployment location.

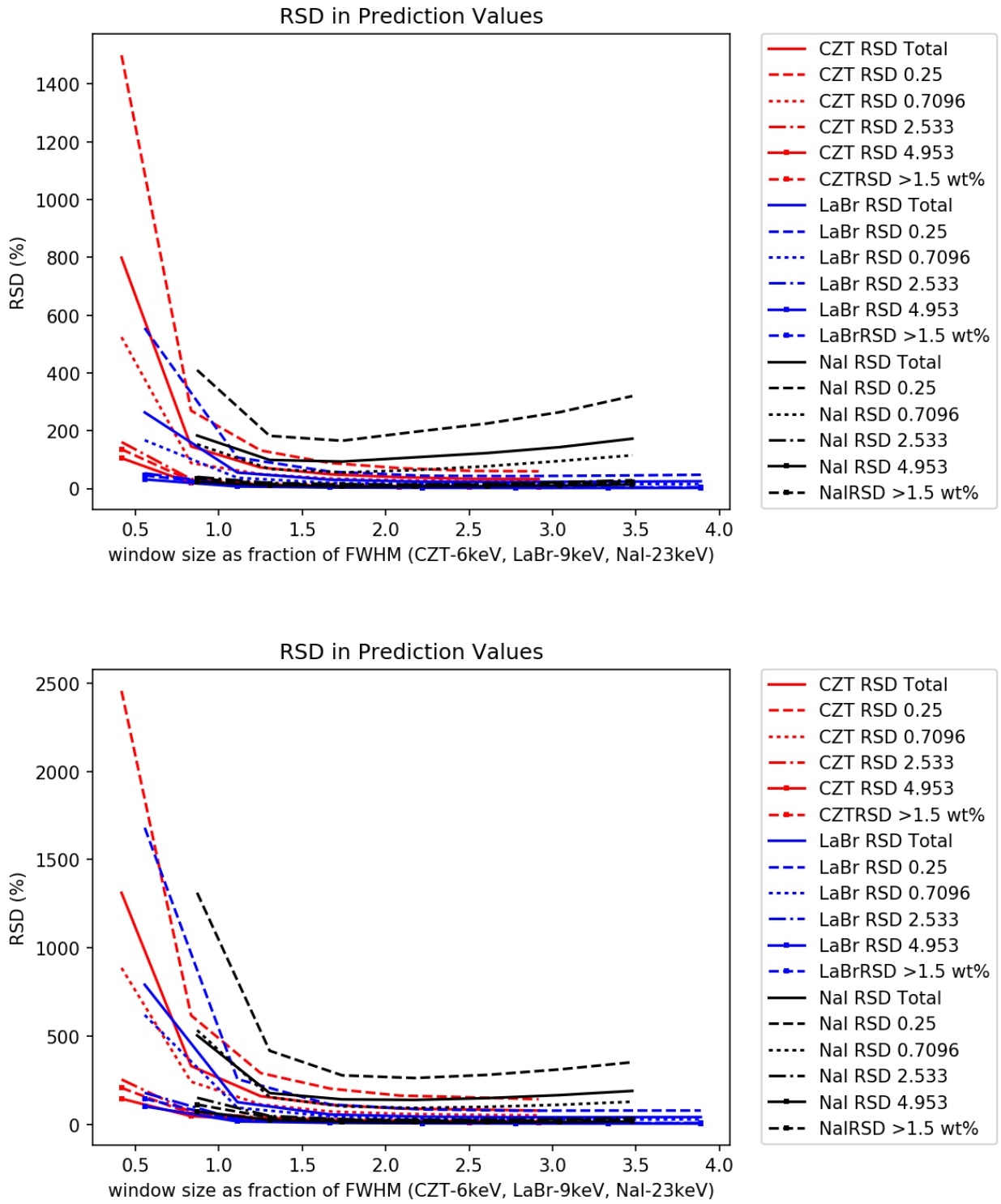

Figure 44. RSD by enrichment with Poisson noise from a 5-minute collection (top) and 1-minute collection (bottom).

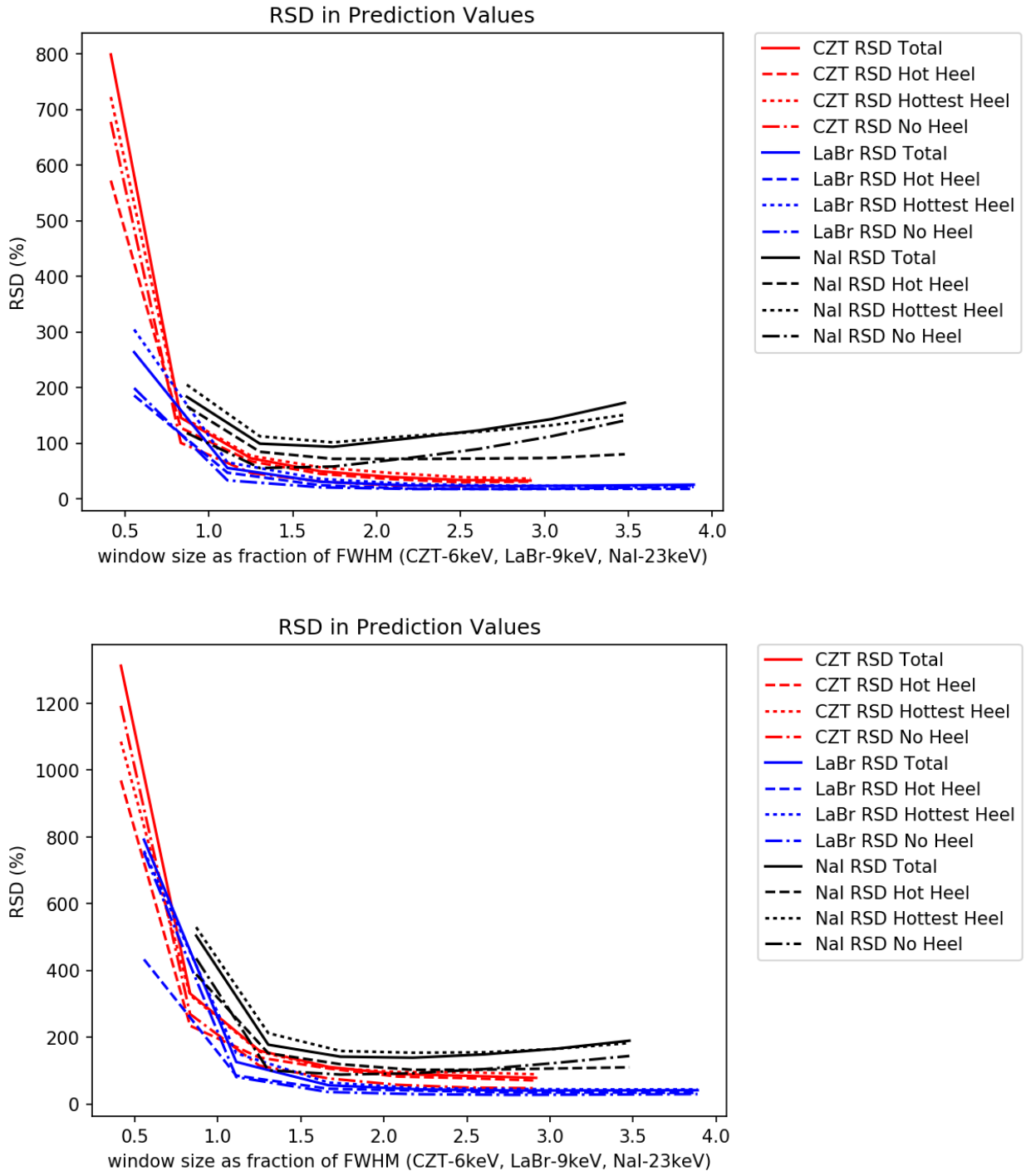

Figure 45. RSD by heel type with Poisson noise from a 5-minute collection (top) and 1-minute collection (bottom).

It is important to note, however, that the RSD values in Figure 44 and Figure 45 are only based on the spectra for which the 186-keV peak was clearly identified (i.e., a signal greater than 3-sigma above statistical noise) and then analyzed using the SWC to separate the signal in that peak from the noise. An unattended enrichment-meter instrument must be robust to statistical noise in a way that allows

identification of the correct peak with high frequency, regardless of the signal to noise ratio. One measure of this robustness is the measured variation in the channel identified to be the midpoint of the 185.7 keV peak. For these simulated spectra, the exact channel corresponding to 185.7 keV is known and therefore, can be compared to the midpoint channel asserted by the peak-searching aspect of the SWC method. Again, the lowest enrichment and hottest-heel cylinders exhibit the poorest performance, and it is likely that this misidentification of the peak channel is a contributor to the RSD in the previous figures for every window size. A key finding from the channel-deviation analysis is that the LaBr has the best performance, assuming the inter-detector comparison is made at the most suitable window size for each specific detector (as discussed previously: NaI ~2.5*FWHM, LaBr and CZT ~2.5*FWHM). LaBr's balance between collection efficiency and energy resolution produces this strong performance. The degraded CZT peak identification (particularly for 1-minute acquisition times and NU/DU cylinders) stems from its low collection efficiency; for NaI it is the lower energy resolution that reduces performance.

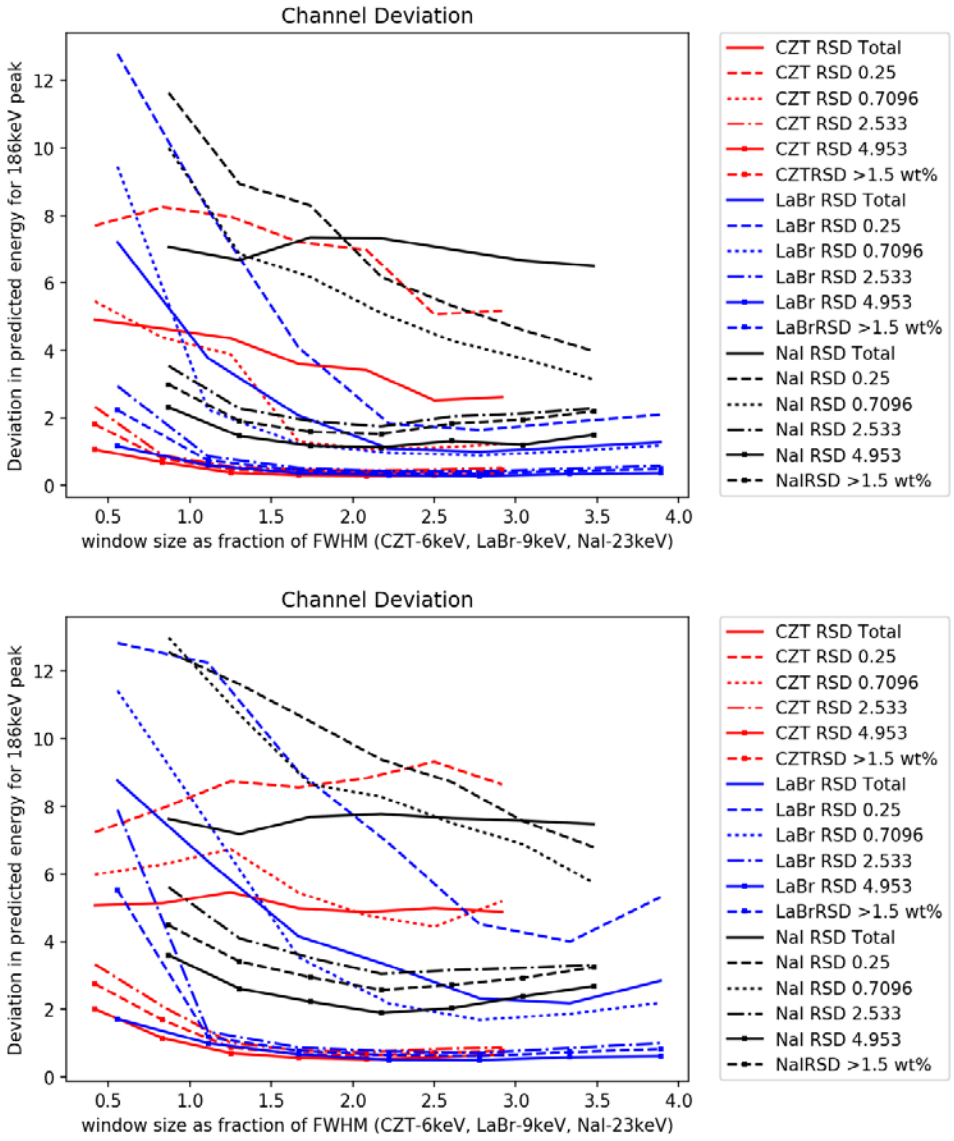

Figure 46. Deviation (in keV) for predicted 186-keV peak midpoint assuming 5-minute collection (top) and 1-minute collection (bottom).

Another figure of merit to examine, relevant to the robustness of a detector/algorithm combination for unattended field use, is the fraction of spectra for which no peak was detected. These non-detections are directly related, operationally, to the number of cylinders that must be either measured again or measured for a longer duration. Figure 47 compares the non-detect probability for the three detector types as a function of FWHM. These plots indicate that LaBr again provides the most consistent performance, assuming that the detectors are compared at the window size commensurate with best RSD performance (i.e., 2.0*FWHM for NaI, ~2.5*FWHM for LaBr and CZT). For the 5-minute occupancies, non-detect fractions for all cylinder enrichments is less than a few percent for LaBr but can be 10% or higher for DU cylinders with CZT and NaI. For the 1-minute occupancies, non-detect probabilities for all detectors are higher but the same basic trends apply. The exception is the LaBr performance for DU cylinders, which actually lags behind CZT. This is a somewhat surprising result and needs further investigation.

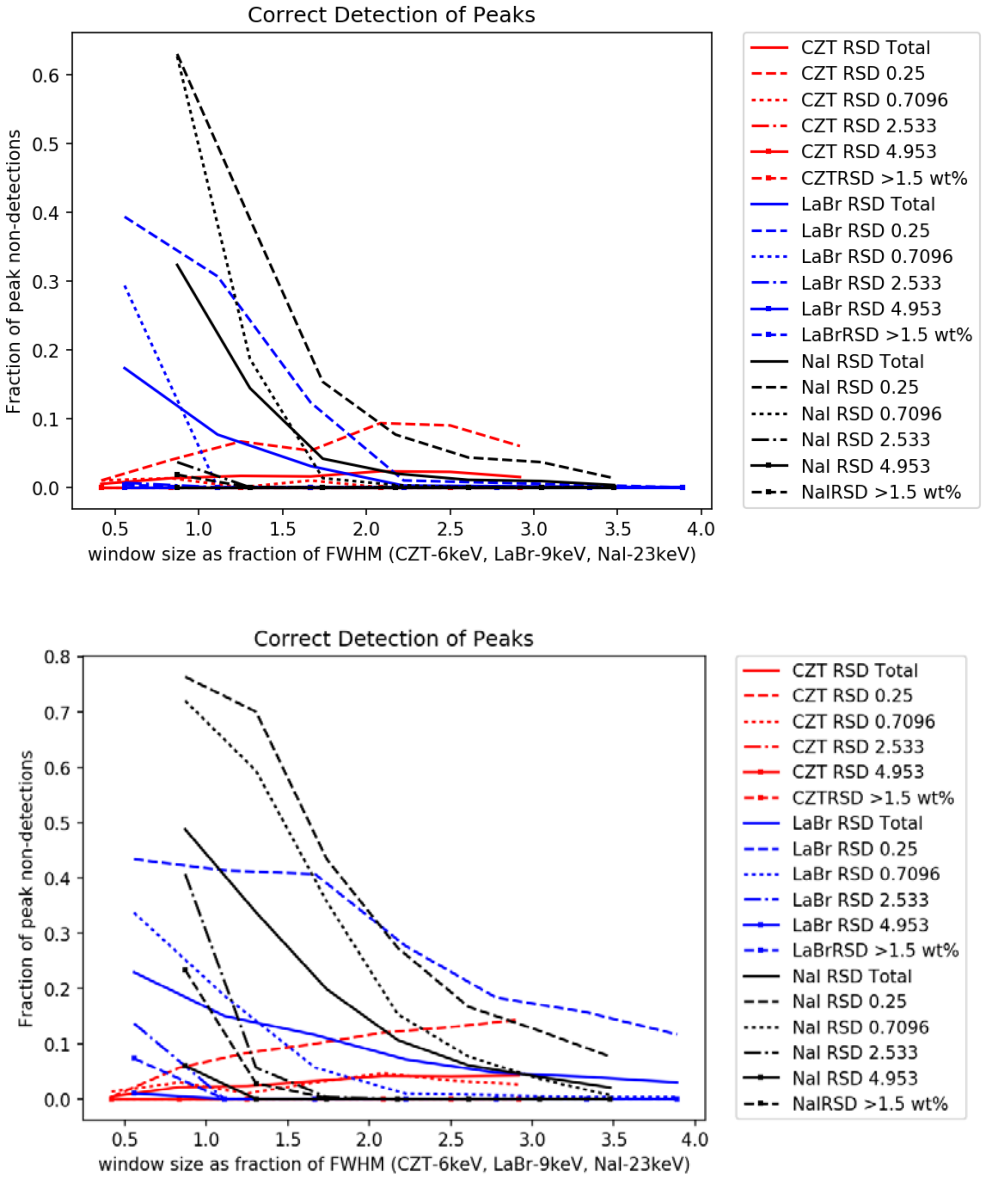

Figure 47. Fraction of spectra without peak detection with Poisson noise from a 5-minute collection (top) and 1-minute collection (bottom).

The peak position deviation and non-detect fractions in Figure 46 and Figure 47 are somewhat discouraging in view of the operational implications for unattended analysis. But it is important to keep in mind that the population of simulated cylinders on which this analysis is based is a worst-case in terms of the fraction of hot and very-hot heel cylinders that tend to degrade peak identification performance. So, while these figures provide a useful relative comparison of peak-identification performance for the three detector types, it is anticipated the non-detect performance for realistic cylinder populations, in the absolute sense, would be better than indicated here.

4.2.4 Summary of Spectrometer Comparison Findings

The figures in the previous sections provide comparison of detector-type performance over a broad range of SWC window widths, which is a useful way to present the data for diagnostic purposes. But a less-cluttered picture of the relative performance of the detector type emerges when it is assumed that the SWC window size is set in a detector-specific fashion, and tuned to achieve the lowest RSD across all relevant enrichment and heels levels (i.e., NaI ~ 2.0*FWHM; LaBr and CZT ~ 2.5*FWHM). This approach is representative of how the SWC algorithm would be deployed in the field. It should also be noted that there may be some tension between the SWC window size that achieves the lowest RSD, and the window size that achieves the best peak identification and non-detect fraction.

Figure 48 provides a summary of the enrichment-meter performance predictions for HEVA-NaI versus the Phase II LaBr and Phase II CZT, for the four enrichment levels and occupancy durations analyzed in this study. The SWC algorithm is the analysis method for all results—other algorithms may produce different results, as discussed later in the section on NaIGEM testing. Key observations from the SWC-based performance predictions in Figure 48 are discussed here.

For the infinite-occupancy-duration case (top), the CZT detector significantly outperforms both LaBr and especially NaI. This trend is most evident for the DU and NU cylinders and is consistent with expectations since the performance price of CZT's low collection efficiency is not realized in the no-noise scenario.

For the more realistic UCVS occupancy durations of 5 minute (middle) and 1 minute (bottom), LaBr is the clear performance winner, due to the balance it strikes between energy resolution and collection efficiency. The superiority of LaBr over CZT is most clear in the DU and NU categories, which is where the greatest improvement in enrichment-meter performance is needed in Phase II.

Compared to the HEVA-NaI performance, both of the candidate Phase II module designs are clearly superior, particularly for the NU and DU cylinders. RSD values for NU and DU are approximately three times lower for LaBr than for NaI for these heel-heavy simulated cylinder populations. This is perhaps the most important and encouraging finding from the comparative study, and provides the necessary data on which to base deployment decisions in Phase II.

While the library of synthetic spectra generated for this study is quite useful for highlighting relative detector performance for the low enrichment, high-heel cylinders, the absolute RSD values shown in Figure 48 should be viewed with caution. As stated earlier, the fact that the spectral populations are based on only three cylinder variants (i.e., no heel, hot heel and very hot heel) at each enrichment means that these populations are likely on the worst-case end of the reality continuum. That is, real cylinder populations are likely to have a smaller fraction of cylinders with a very hot heel and therefore, the RSD values in Figure

48 are likely to be higher than what will be realized in Phase II field trials. This is especially true for the DU and NU cylinder populations where the 186-keV signal is weak. As semi-quantitative support for this assertion, consider the calculated HEVA-NaI RSD values for the three simulated cylinder categories, as compared to the IAEA's International Target Values (ITVs) for a handheld NaI using the enrichment-meter method. For the simulated cylinder populations, the RSD values for HEVA-NaI are 12% for LEU, 56% for NU and 166% for DU, assuming a 5-minute occupancy. The ITVs, based on real-world cylinder populations, NaI spectrometers and a 5-minute measurement time, are 5.8%, 10% and 22% (Zhao 2010). In the Phase I field trial, the HEVA-NaI consistently produced an RSD of 5-6% on all sets of LEU cylinders, another strong indicator that the absolute values of predicted performance in this study are notably pessimistic compared to what is likely in the Phase II field trial and actual IAEA implementation.

Also important to point out is that the benefit of multiple detectors in the UCVS prototype is not considered in this analysis. That is, the enrichment-meter performance estimates are based on only one detector whereas in practice, the results from multiple UCVS gamma-ray modules are likely to be combined when reporting calculated cylinder enrichment.

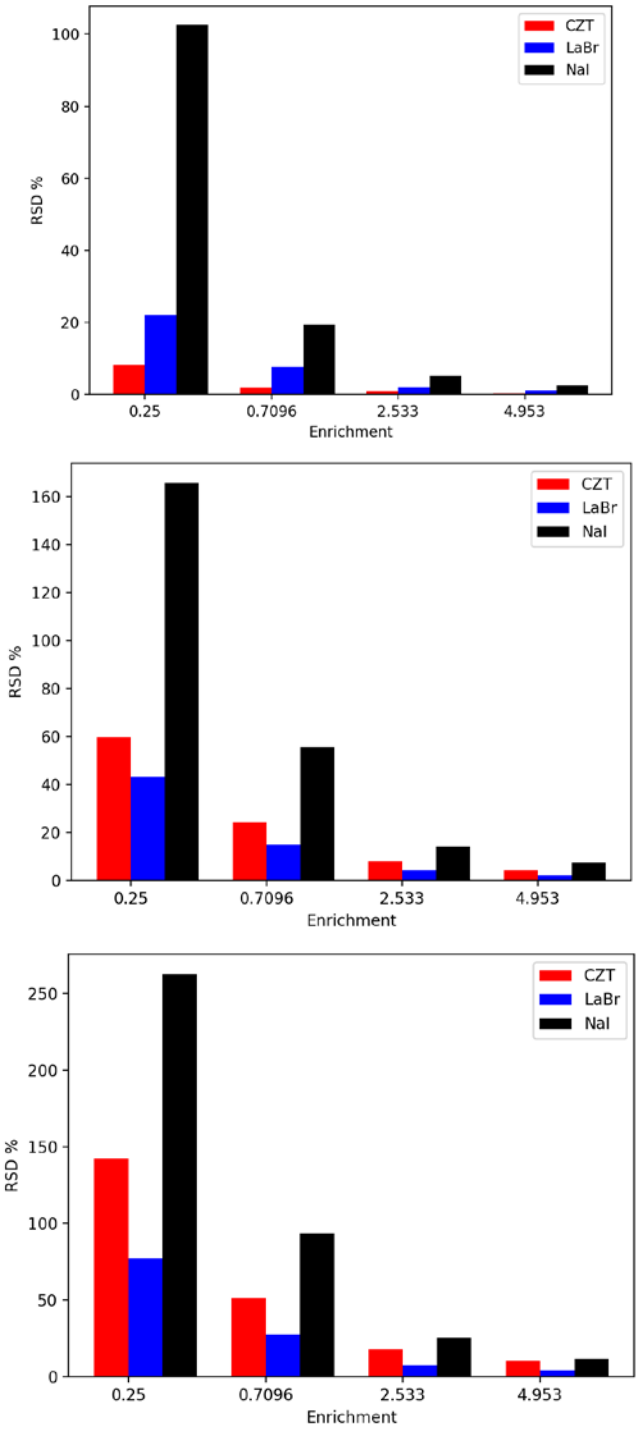

Figure 48. Aggregated RSD values detector and enrichment for cylinder populations with equal distribution of no-heel, hot-heel and very hot heel cylinders. Three occupancy durations are considered: infinite-time (top), 5-minute (middle), 1-minute (bottom).

4.3 Initial Evaluation of NaIGEM for UCVS Scenario

NaIGEM is a gamma-ray analysis software used in several commercial detector systems for uranium enrichment analysis, including the attended cylinder verification activities performed by the IAEA and Euratom. In the case of the IAEA deployments, NaIGEM runs on FLIR's HM-5 detector. Originally developed for NaI, NaIGEM is now also adapted for LaBr. The IAEA has taken responsibility for further developing NaIGEM, since the author, Ray Gunnink, is retired. PNNL acquired version 2.1.4 (latest) of the program directly from Dr. Gunnink (gammaray@comcast.net) and communicated with Dr. Gunnink to ensure that the calibration and analysis parameters used by PNNL in the analysis presented here are consistent with those used by the IAEA for handheld, attended cylinder verification.

Note that, in contrast to the comparative performance study described earlier that was based entirely on simulated gamma-ray spectra, this initial NaIGEM evaluation was based entirely on measured cylinder spectra from the Phase I field trial, more specifically the center HEVA module (HEVA-2 in the Phase I report). PNNL staff calibrated the NaIGEM parameters based on UF_6 spectra from Phase I and processed all of the 229 cylinder spectra included in the Phase I 'Typical All' population.

Because NaIGEM requires spectra in formats other than the N42 format in which the Phase I field trial data was collected, PNNL converted the spectra into SPE files with the PeakEasy program. When each N42 file for a particular cylinder occupancy is converted, six SPE files are created corresponding to the occupancy and background spectra for each of the three HEVA modules in the Phase I prototype. Since NaIGEM is currently limited to analyzing spectra of 1024 channels or less, the Phase I spectra (collected at 8192 channels extending to approximately 10 MeV), were truncated to 1024 channels via another feature in PeakEasy during the conversion process to SPE files. Once the spectra were readable by NaIGEM, input parameters were set to describe the cylinder measurements, namely: the uranium material, the container wall material and thickness, the detector thickness, the collimator diameter and thickness, and the gain and offset parameters. These parameters are shown in the screen-shot of the NaIGEM graphical user interface in Figure 49. The cylinder spectra in the NaIGEM analysis were not background-subtracted, consistent with the way in which the Phase I SWC analysis was performed and with the fact that the background intensity is essentially negligible compared to the signals during a cylinder occupancy.

The next step was to determine a calibration factor (basically the efficiency of the detector for 186 keV photons for a given enrichment). This is done by selecting one or two spectra taken from a calibration standard and entering the known enrichment. Since no such standards were measured in Phase I, a 4.95 wt.% cylinder known to have relatively low wall deposits was taken as the calibration cylinder.

The results from PNNL's NaIGEM analysis of the Typical All spectra are shown in Table 4, and compared to the SWC results for the same sets of cylinders: all 229 including the three NU cylinders; 226 excluding the NU cylinders. These results indicate that the SWC algorithm consistently outperforms NaIGEM, including for the NU cylinders.

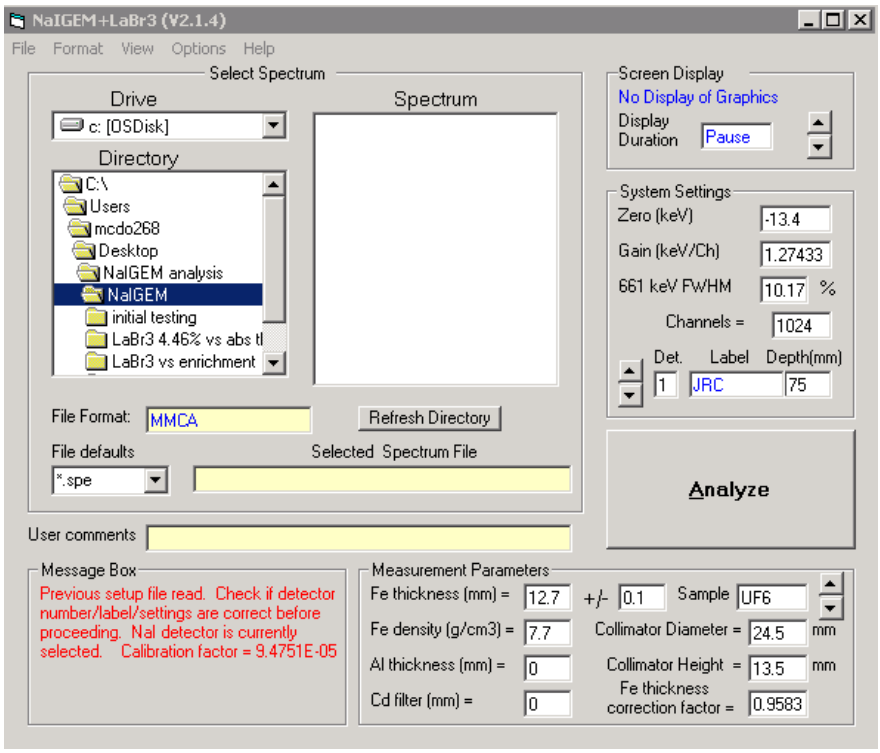

Figure 49. Screenshot of the NaIGEM program user interface, including the parameter settings used in the analysis of the Phase I HEVA-NaI spectra.

Table 4. RSD (one-sigma) results in enrichment for the SWC and NaIGEM algorithms for the Typical All Phase I population. Results for all 229 cylinders (including three NU cylinders) and the 226-cylinder set that excludes those NU cylinders are shown.

Typical All cylinders	SWC	NaIGEM
All cylinders	6.7	9.7
Cylinders > 1.5 wt%	5.9	8.8

To build confidence that PNNL was properly setting NaIGEM parameters and therefore, achieving the expected performance from the algorithm, PNNL provided Dr. Gunnink with a subset of the Typical All spectra, 22 in all. Dr. Gunnink performed an independent analysis of those 22 cylinders, using the same calibration cylinder, and a comparison of the two sets of results showed that PNNL's analysis obtained very similar results to Dr. Gunnink's analysis.

An important feature of NaIGEM is that gain, offset, and resolution changes among spectra are automatically accounted for in the analysis. In this exploratory analysis by PNNL, these parameters were set based on the 4.95 wt% calibration cylinder and used for all 229 cylinders in the Typical All population. The offset and gain values for those 229 Typical All cylinders for the middle Phase I HEVA module, as calculated by PNNL's SWC algorithm for the same spectra fed to NaIGEM, are shown below in Figure 50.

The offset results indicate relatively consistent behavior over the course of the 8-month field trial, with the exception of one cylinder (approximately number 195 in Figure 50), in which the offset is substantially different. Further investigation is needed to understand this outlier. For the gain values, there is some evidence of long-term drift in the middle HEVA module over the course of the 8-month field trial.

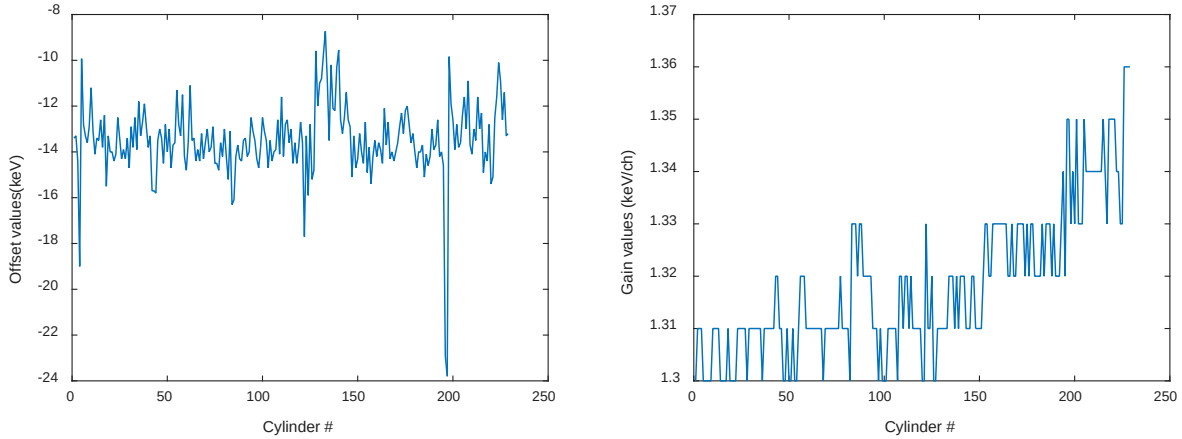

Figure 50. Plots of asserted offset (left) and gain (right) for the measured HEVA-2 spectra from 229 Typical All cylinders.

Figure 50 characterizes the offset and gain for the input spectra to NaIGEM, but it is not yet clear whether NaIGEM is capable of automatically accommodating this level of variance in those parameters, and still achieve optimal results. A preliminary probe into that question compared the RSD for the first 125 cylinders in the population, where gain drift is minimal, to the RSD for the remaining 104 cylinders where gain drift is more significant. The RSD values for those two subpopulations are nearly identical, indicating that PNNL's calibration approach was reasonably robust.

Future work should consider the impact of different calibration cylinder sets on performance, compare NaIGEM performance when individual gain/offset parameters are given for each spectrum (rather than just for the calibration spectrum), and automate NaIGEM processing for unattended use.

5.0 Evolution of Content Re-Verification Concept

There are several questions beyond the verification of declared enrichment and ^{235}U mass that the UCVS NDA signatures may be able to wholly or at least partially address. First, "Is there any set of measurements that allow verification that contents of a cylinder are the same as previously encountered?" Second, "Is there a set of measurements that allow us to determine whether or not a cylinder has been tampered with since the last time it was observed?" For the latter question, no data is available to study cylinders that have had material removed or inserted. The former, to be called Content Re-Verification (CRV), can be broken into secondary questions, for example the susceptibility of the measurement system to small perturbations in cylinder placement, and the uniqueness of specific NDA signatures emitted by a cylinder.

In Phase I, PNNL and LANL examined these questions using single parameters, for example the 1001-keV ROI or the singles neutron signature. In this section, PNNL uses the same, rather limited, set of CRV-related Phase I field trial data to preliminarily explore multi-dimensional CRV methods. While far from comprehensive or definitive, this work will inform the planning of CRV-related measurements and analysis in Phase II.

5.1 Phase I CRV Data Collection Procedures and Descriptions

An overview of the Phase I CRV-related field data is provided in Table 5, using proxy cylinder IDs. Table 5 describes the set of tests intended to explore the variability of various NDA signatures with specific changes in cylinder-sensor geometry, for example shifts, flips and rotations of the cylinder relative to the UCVS platform.

Table 5. Overview of geometry-specific Content Re-Verification (CRV) field data from UCVS Phase I. For each of the 5 cylinders of the given enrichments, the number of geometry-related events is tabulated.

Cylinder ID	# Exact Replacements	# Shifts	# Flips	# Rotations	Declared Enrichment
0	3	2	1	1	1.544
1	3	2	1	1	4.95
2	8	4	2	2	1.797
3	5	2	1	1	3.201
4	4	2	1	1	4.978

In this study, a total of 47 occupancies spanned five distinct cylinders in five separate geometric configurations. For each occupancy, the NDA signatures under study are the 186-keV, 1001-keV, and high-energy non-traditional neutron (i.e., 3-8 MeV, hereafter "NT") regions for each of three Phase I HEVA modules, as well as an alternative measurement of the 186-keV region of interest obtained via the SWC method described earlier.

Each "Exact Replacement" measurement of a cylinder is obtained by lifting the cylinder away from the platform, then returning it immediately to the platform while carefully aligning the platform supports with marks on the cylinder itself. Shifts involve moving the cylinder 10 cm laterally in either direction on the

platform. Flips involve spinning the cylinder about the axis perpendicular to the axis of symmetry by 180 degrees; rotations involve rolling the cylinder by approximately 45 degrees about the axis of symmetry. Full descriptions of the geometry-variation tests in Phase I can be found in the UCVS Phase I final report (Smith 2016). Note that in most of the scoping analyses described below, only the HEVA-2 module (H2 in this section) is included for simplicity and to illustrate the analysis concepts but in practice, the CRV method will be applied across multiple detectors.

5.2 Multi-dimensional Reverification: Scoping Analysis

A pair-wise mapping of the four candidate NDA signatures analyzed in the scoping study is given in Figure 51, for all of the CRV occupancy types: exact replacements, shifts, flips and rotates. These plots show clear clustering by cylinder for most of the pairs for the exact replacements and shifts, but significant scatter for several of the more-dramatic geometry changes, i.e., rotates and flips. This variability likely arises from the variability in the spatial distribution of wall deposits in the cylinders, supported by the observation that the 186-keV and 1001-keV ROIs, as gross-count ROI regions driven in whole or part by ^{238}U daughter emissions, are more tightly coupled to cylinder wall deposit distribution than enrichment. The NT and SWC, signatures, on the contrary, show relatively tight clustering by enrichment, as expected since they are, in theory, directly proportional to enrichment (assuming a full cylinder).

A key question to be investigated in the CRV analysis is whether sequential verifications of a cylinder, for example days or weeks apart, can be statistically coupled to the initial verification of that same cylinder. All data for this analysis has been rescaled via a Min-Max scaling method (i.e., forcing the range to lie between 0 and 1). This rescaling ensures that our analysis does not determine that any single feature is a significant indicator due to differences in the absolute count rate of each region and does not disturb the variances of the measurements clusters produced by individual cylinders. Toward this question, a statistical test called the Kolmogorov-Smirnov (KS) test was applied to determine the likelihood that two measurements were drawn from a statistical distribution with the same mean. In this analysis, it is assumed that the data points associated with a single cylinder are realizations of a single Poisson distribution and that the distribution can be estimated using the mean value of the cluster of data points considered in the analysis. In this case, only the exact replacements and shifts for a given cylinder were taken as independent sequential verification measurements of the same cylinder (in the field tests these moves were separated by only minutes). The flips and rotates shown in Figure 51 were removed because they are known to be outliers in terms of sensor-cylinder geometry.

Table 6 summarizes the initial results from the KS tests on the Phase I geometry-perturbation data represented by the exact replacements and shifts. An ‘R’ indicates rejection of the hypothesis that two sets of measurements have been obtained from the same distribution. It is assumed that the KS statistic must exceed 0.8 with p-value less than 0.01 in order for rejection. A blank entry indicates that there is insufficient evidence to reject the hypothesis and that the measurements could have come from the same cylinder.

This test showed that for the SWC measurements alone, cylinders 0 and 2 were easily confused as were cylinders 1 and 4. This is consistent with the fact that the enrichments of those cylinder pairs are similar—and the SWC signature is directly proportional to enrichment. A similar test on the measurements from the NT signal indicated again with high confidence that Cylinders 1 and 4 are easily confused, but all of the other cylinders can be distinguished. The KS test does indicate high confidence that all of the SWC measurements from cylinder 3 are distinct from any of the other clusters.

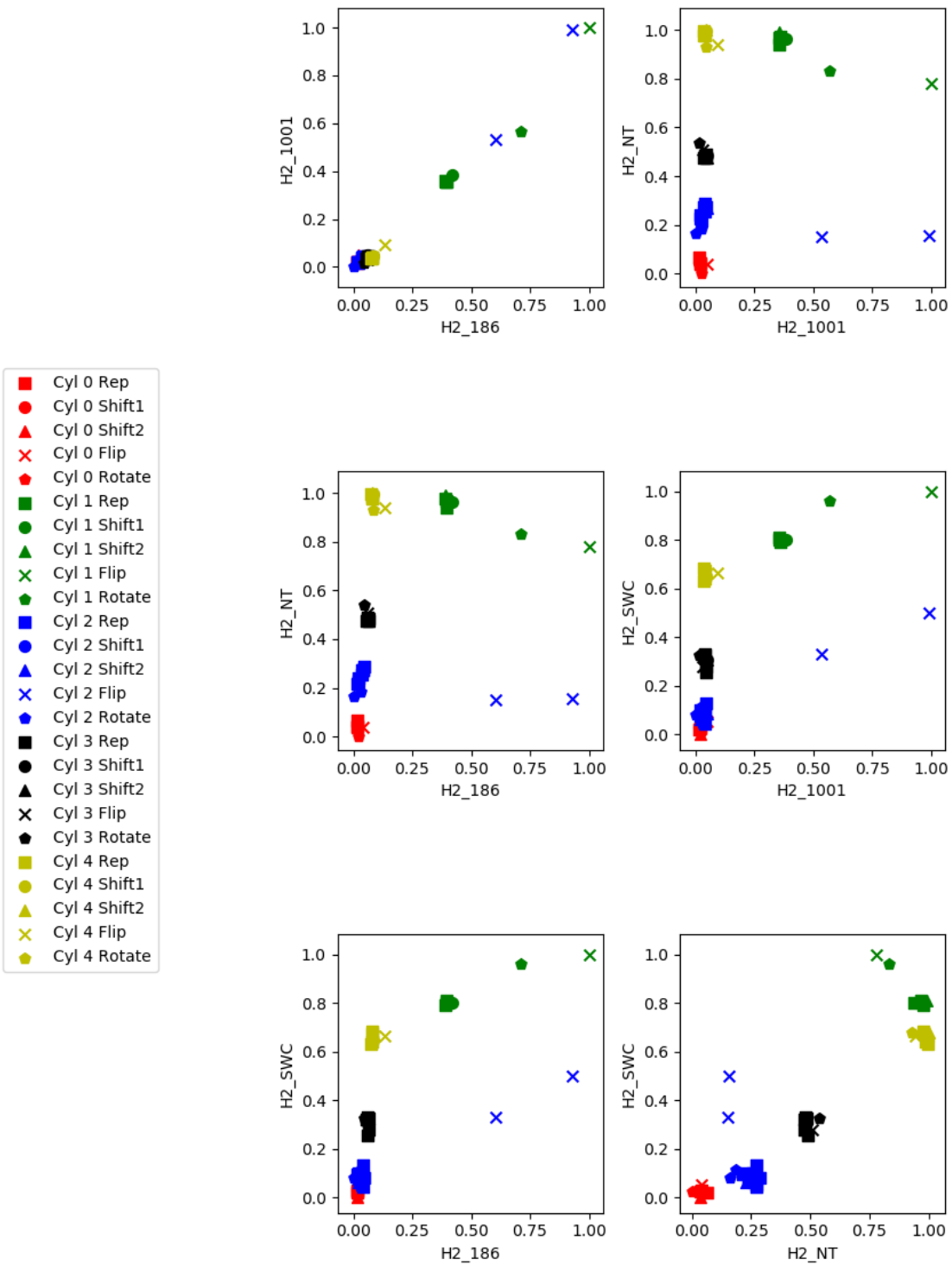

Figure 51. Pairwise plots of candidate CRV signatures illustrating inter- and intra-cylinder variability. All potential feature regions have been rescaled using a MinMax scaling method to avoid over-emphasizing the importance of any particular region due to difference in net count rates.

Table 6. Results of the Kolmogorov-Smirnov Test. Across the horizontal is the true distribution from which the cylinder-specific measurements were taken. The vertical states the set of measurements under test. An 'R' indicates that the hypothesis was rejected; green boxes indicate tests that accurately support the hypothesis; yellow boxes indicate cases where the hypothesis was inaccurately supported.

Cylinder	Cyl 0 SWC	Cyl 0 NT	Cyl 1 SWC	Cyl 1 NT	Cyl 2 SWC	Cyl 2 NT	Cyl 3 SWC	Cyl 3 NT	Cyl 4 SWC	Cyl 4 NT
0			R	R		R	R	R	R	R
1	R	R			R	R	R	R		
2		R	R	R			R	R	R	R
3	R	R	R	R	R	R			R	R
4	R	R			R	R	R	R		

The exploratory analysis presented above is preliminary and based on limited data that is far from ideal for such a test (e.g., the shifts included in the population may indeed represent the kind of change that the CRV hypothesis test should reject). In further studies, the KS test could be used to determine whether a new measurement is distinct from all previous measurements. If information regarding whether a cylinder has been previously measured is incorporated, then this test could be used to alert to tampering by determining whether a new measurement is consistent with previous measurements. Given more examples of cylinders of similar type, thresholds and confidence levels to determine cylinder uniqueness could be determined.

In order to focus on the inter-cylinder variability in the candidate signatures in a way that removes the systematic variation due to enrichment, all of the Phase I CRV measurements were scaled in the following way: exact replacement measurements (x) were used to calculate the mean (m) and standard deviation (s) for each of the candidate signatures independently. Those mean and RSD values were then used to rescale with the standard z-score (x-m)/s for all measurements for the shifts and replacements, as seen in Figure 52. This normalization method is similar to the one employed in the Phase I CRV analysis, but now it is applied in two-dimensional sets of the candidate NDA signatures. Observations from Figure 52 include:

- Rescaling in this fashion with so few measurements forces an artificial variance on the data, but even still, small shifts in the measurement position and by extension the spatial variation in the wall deposits, are readily discernible.
- Using HEVA-1 and HEVA-3 for any signature (although it is most obvious for the 1001-keV ROI), the direction and distance of the shift are clear, due largely to the fact that these detectors are positioned near the ends of the cylinders and even small shifts remove cylinder material from their field of view. It will be important, therefore, to ensure that the gamma-module field of view is fully filled by the cylinder in future tests and trials, to avoid confusing geometric perturbations and cylinder-contents perturbations.

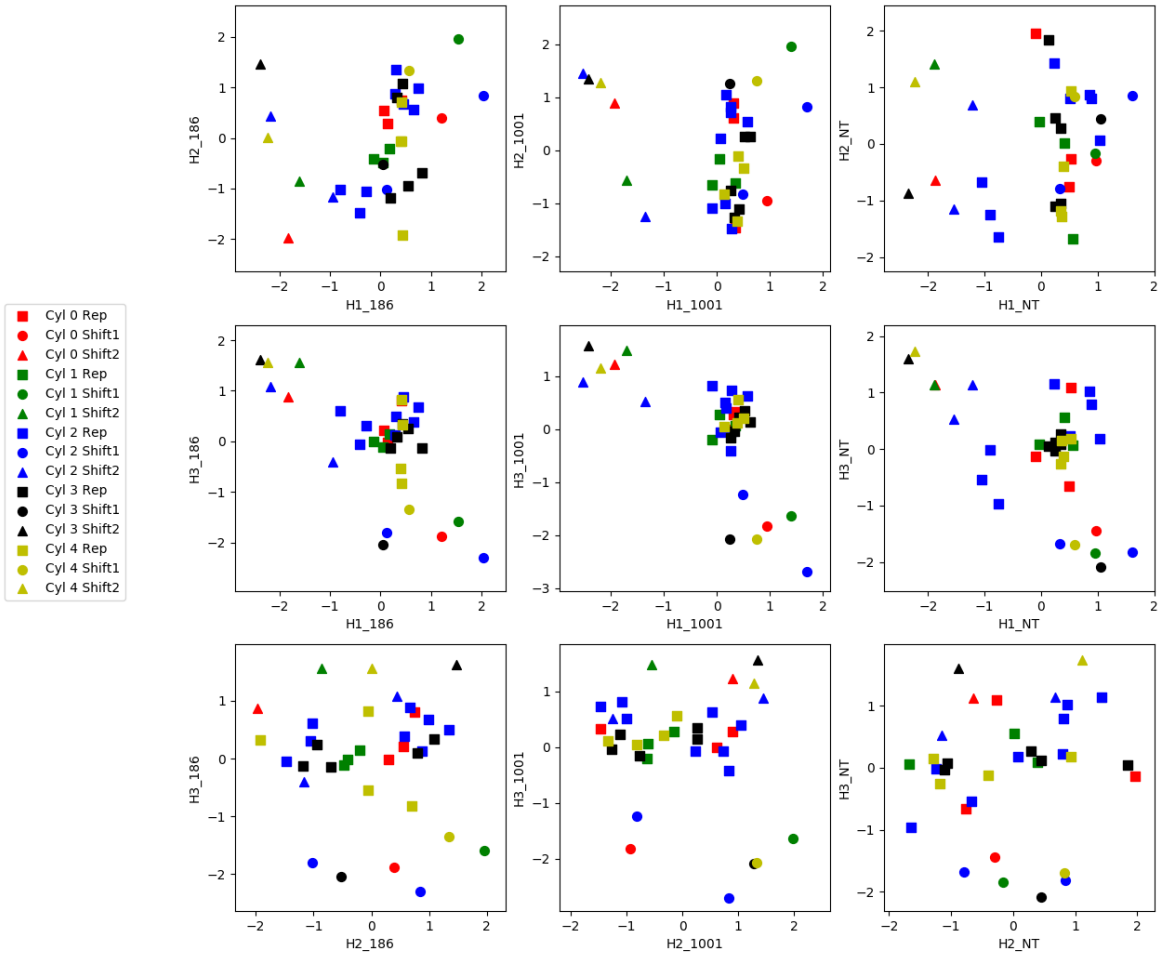

Figure 52. Multi-detector measurements rescaled by Z-score to remove dependencies on cylinder enrichment and examine the expected variability of cylinder measurements.

The limited Phase I CRV data provides a useful starting point for investigation of the CRV concept, but in order to determine whether the envisioned analysis methods are effect for large cylinder populations, the Phase II experimental design should consider the following:

- Daily calibration measurements for a single known cylinder (e.g., 4.95 wt%) for as many days as possible – this would provide more information on the expected geometric and temporal variability of the candidate signatures and therefore higher confidence than the relatively few exact replacement measurements, usually collected in a very short time frame in Phase I could provide.
- 10-15 exact replacement measurements of 3-4 cylinders that most closely match the calibration cylinder measurements (or at very least, each other) – this would provide more information on wall-deposit spatial variation and other inhomogeneities among cylinders of the same enrichment.

6.0 Summary

A cornerstone activity in this bridge scope between UCVS Phases I and II was a design study for a Phase II gamma-ray module that is significantly more compact than the HEVA modules deployed in Phase I, and that can be positioned along the bottom third of the cylinder (alongside neutron modules) to facilitate a standard geometry for both Type 30B and Type 48 cylinders in Phase II. In FY17, PNNL designed and developed two LaBr-based prototype modules that are significantly more compact than the HEVA modules fielded in Phase I, and are expected to be suitable for the stand-alone and modular UCVS configurations envisioned for Phase II. Preliminary laboratory testing, including the refinement of the Osprey pulse-processing parameters for the characteristics of the LaBr spectrometer, was completed.

Using measured cylinder data from Phase I to benchmark spectrometer responses and define the potential range of wall-deposit contributions, PNNL employed MCNP to develop a large library (hundreds) of synthetic cylinder spectra for LaBr (3.8cm×3.8cm) and CZT (1600mm^3 based on μSPEC 1500 from RITEC) spectrometers in a compact tungsten collimator module compatible with the nominal Phase II UCVS design, and a NaI (7.5cm×7.5cm as in Phase I) spectrometer in the as-deployed Phase I HEVA configuration (i.e., iron/poly collimator to encourage indirect neutron detection). Occupancy durations ranged from infinity to 1 minute. These synthetic spectra were used to adapt PNNL's square-wave-convolute (SWC) algorithm to the higher resolution of LaBr and CZT (Phase I included only NaI) and then to compare the anticipated performance of LaBr, CZT and NaI over a range of enrichments, with a focus on NU and DU cylinders.

PNNL's simulation-based analysis indicates that compared to the HEVA-NaI performance, both of the candidate Phase II module designs (i.e., LaBr and CZT) are clearly superior for anticipated UCVS occupancy durations, particularly for the NU and DU cylinders. RSD values for NU and DU are approximately three times lower for LaBr than for NaI for these heel-heavy simulated cylinder populations; CZT performance gains are somewhat lower but still notable. For the occupancy durations envisioned for UCVS (i.e., less than 5 minutes) LaBr is substantially superior to CZT, due to the balance that LaBr strikes between energy resolution and collection efficiency. The superiority of LaBr over CZT is most clear in the DU and NU categories, which is where the greatest improvement in enrichment-meter performance is needed in Phase II. The key finding from this comparative investigation is that a side-looking LaBr spectrometer with an appropriate tungsten collimator, and coupled to PNNL's SWC algorithm, should produce significantly improved performance for NU and DU cylinders, when compared to the NaI-based HEVA module fielded in Phase I.

In the application of NaIGEM to the UCVS Phase I HEVA-NaI spectra for the Typical All population, it was demonstrated that PNNL's SWC algorithm outperformed NaIGEM, including for the NU cylinders. This preliminary finding encourages further comparative evaluation of these two candidate enrichment-meter algorithms for NaI and LaBr spectrometers—scope that was included in the UCVS Phase II proposal to the IAEA. If the initial indications of improved performance by SWC in the UCVS unattended scenarios are proven to be robust, it is also possible that the IAEA would be interested in testing of the SWC algorithm for attended, handheld verification measurements (which currently use NaIGEM).

7.0 References

Broughton, D. P. and M. T. Swinhoe. 2017. "Re-evaluation and assessment of potential correction factors for PNEM enrichment and ^{235}U mass calibrations." LA-CP-17-20346. Los Alamos National Laboratory.

Cooley, J. N, "Model Safeguards Approach and Innovative Techniques Implemented by the IAEA at Gas Centrifuge Enrichment Plants," in *48th Annual Meeting of the Institute of Nuclear Materials Management (INMM)*, Tucson, AZ, 2007.

Ivanov V., J. Mintcheva, A. Berlizov and A. Lebrun. 2015. "Performance Evaluation of New Generation CdZnTe Detectors for Safeguards Applications," IAEA-CN-220, IAEA.

Kulisek, J. A, J. K. Hartwell, M. E. McIlwain, and R. P. Gardner. 2007. "Design and Preliminary Monte Carlo Calculations of an Active Compton-Suppressed $LaBr_3$(Ce) Detector System for TRU Assay in Remote-Handled Wastes," *Nuclear Instruments and Methods in Physics Research A*, vol. 580, pp. 226-229.

Lebrun, A., S. C. Kane, L. Bourva, S. Poirier, N. E. Loghin, and D. Langlands, "Improved verification methods for safeguards verifications at enrichment plants," in *Advancements in Nuclear Instrumentation Measurement Methods and their Applications (ANIMMA), 2009 First International Conference on*, 2009, pp. 1-8.

Quarati, F.G.A, et al. 2012. "Study of ^{138}La radioactive decays using $LaBr_3$ scintillators." *Nuc. Inst. & Meth.* A, vol. 683, pp. 46-52.

Richter, M. and P. Siffert. 1992. "High resolution gamma ray spectroscopy with CdTe detector systems." *Nuc. Inst. & Meth.* A, vol. 322, pp. 529–537.

Schlesinger, T. E. and et al. 2001. "Cadmiun Zinc Telluride and Its Use as a Nuclear Radiation Detector Material," *Materials Science and Engineering*, vol. 32, pp. 103-189.

Smith, L. E., A. R. Lebrun, and R. Labella, "Potential Roles of Unattended Safeguards Instrumentation at Centrifuge Enrichment Plants," *Journal of Nuclear Materials Management*, 2013.

Smith, L. E., K. A. Miller, E. K. Mace, D. V. Jordan, J. Morrissey, C. R. Orton, C. D. Rael, R. Veldhof, and T. Visser. 2014. *A Study of Candidate NDA Methods for Unattended UF_6 Cylinder Verification: Action Sheet 40 Final Report.* PNNL-22954, Pacific Northwest National Laboratory, Richland, Washington.

Smith, L. E., D. V. Jordan, J. A. Kulisek, B. S. McDonald, and E. K. Mace, "Viability of UF6 Cylinder Verification using the Hybrid Enrichment Verification Array (PNNL-SA-102233)," *Journal of Nuclear Materials Management (submitted)*, 2015.

Smith, L. E., K. A. Miller, et al., “Viability Study for an Unattended UF6 Cylinder Verification Station: Phase I Final Report,” PNNL-25395, Pacific Northwest National Laboratory, Richland, WA, May 2016.

Sokolov, A., V. Kondratjev, V. Kourlov, F. Levai, and T. Honkamaa. 2008. “CdTe Linear Arrays with Integrated Electronics for Passive Gamma Emission Tomography System.” *2008 IEE Nuclear Science Symposium Conference Record*. N02-221, pp. 999-1002.

United States Enrichment Corporation. “The UF_6 Manual: Good Handling Practices for Uranium Hexaflouride,” USEC-651, Rev. 9, July 2006.

Walton, R., T. Reilly, J. Parker, J. Menzel, E. Marshall, and L. Fields. 1974. “Measurements of UF_6 cylinders with portable instruments,” *Nucl. Technol., vol. 21, no. 2, pp. 133-148*.

Zalavadia, M. A., L. E. Smith, B. S. McDonald, J. A. Kulisek, E. K. Mace, N. S. Deshmukh, “Hybrid Enrichment Verification Array: Module Characterization Studies”, PNNL 25066, Pacific Northwest National Laboratory, March 2016.

Zhao, K. 2010. *International Target Values 2010 for Measurement Uncertainties in Safeguarding Nuclear Materials*. IAEA STR-368, IAEA Department of Safeguards, International Atomic Energy Agency, Vienna, Austria.

Pacific Northwest
NATIONAL LABORATORY

Proudly Operated by **Battelle** *Since 1965*

U.S. DEPARTMENT OF
ENERGY

902 Battelle Boulevard
P.O. Box 999
Richland, WA 99352
1-888-375-PNNL (7665)

www.pnnl.gov